

# Scale-variant Topological Information for Characterizing Complex Networks

Quoc Hoan Tran,<sup>\*</sup> Van Tuan Vo,<sup>†</sup> and Yoshihiko Hasegawa<sup>‡</sup>

*Department of Information and Communication Engineering,  
Graduate School of Information Science and Technology,  
The University of Tokyo, Tokyo 113-8656, Japan*

(Dated: December 15, 2024)

Real-world networks are difficult to characterize because of the variation of topological scales, the non-dyadic complex interactions and the fluctuations. Here, we propose a general framework to address these problems via a methodology grounded on topology data analysis. By observing the diffusion process in a network at a single specified timescale, we can map the network nodes to a point cloud, which contains the topological information of the network at a single scale. We then calculate the point clouds constructed over variable timescales, which provide scale-variant topological information and enable a deep understanding of the network structure and functionality. Experiments on synthetic and real-world data demonstrate the effectiveness of our framework in identifying network models, classifying real-world networks and detecting transition points in time-evolving networks. Our work presents a unified analysis that is potentially applicable to more complicated network structures such as multilayer and multiplex networks.

Characterizing the structure of complex networks is the most fundamental issue in deciphering network dynamics. The network anatomy is quite relevant to phenomena occurring in networks such as spread of information or epidemic disease or robustness under attack. A considerable number of applications have been of great interest in the literature. These applications include controlling and predicting patterns of dynamics in networks [1–3], quantifying structural and functional similarities of biological networks [4–6] and detecting transition points in time-evolving networks [7–9]. In practice, the structure of real-world networks is inherently difficult to characterize. First, real-world networks have complex patterns that are reflected at various topological scales [10–12]. In revealing these patterns, the conventional statistical measures [13, 14] and methods [10, 15–18] remain ill-defined as evidenced by the lack of representation of the variation of topological scales. Second, real-world networks are representations of complex systems that have dyadic and non-dyadic interactions [19–21]. However, most of the current methods for characterizing complex networks focus only on the dyadic interactions such as detecting the existence of pairwise edges or paths connected by successive edges. Third, real-world networks often suffer from fluctuation caused by external factors [22]. Because of the fluctuation, the quest for unifying the principles underlying the topology of networks emerges only in simple idealized models without any additional effect [23–25]. Robust representations under the fluctuation have not been explored for characterizing structures of real-world networks.

In this Letter, we propose a general framework grounded on topological data analysis that characterizes complex networks over variable topological scales. Our framework constructs the scale-variant topological features of complex networks that reflect the variation of topological scales. The framework can provide in-depth

understanding of the complex interactions and the robustness under fluctuation. We theoretically prove that the scale-variant topological features are robust under perturbation applied to the network. By analyzing several network models, we demonstrate that our framework can characterize the parameters that are used to generate the networks. Furthermore, we can distinguish both synthetic and real-world networks with better results than other conventional approaches. We further apply our framework to detect the transition points between the developmental stages of *Drosophila Melanogaster* in the time-evolving gene regulatory networks. Interestingly, these transition points agree with those obtained from the experimental results on the profiling.

The variation of topological scales can be revealed via the topological information obtained along with the diffusion process exhibited in the network. When the diffused time  $\tau$  is small, the microscale structure is revealed as there is almost no information exchanged between the nodes. Increasing  $\tau$  will reflect the mesoscale decomposition of the network until the macroscale structure is finally captured. At each  $\tau$ , we map the network nodes to a point cloud, where a group of close points represents the unit of points that easily exchange information in the diffusion process. To capture the non-dyadic interactions, we construct a simplicial complex model [26] from the point cloud. To obtain a robust representation, we use the topological data analysis [26–29], which is a set of computational topology methods, to encode the simplicial complex model into noise-tolerant quantitative features. Observing these features with varying  $\tau$  provides insights into the variation of topological scales as well as the interplay between the structure and dynamics of the network. Therefore, we construct scale-variant topological features by regarding  $\tau$  as a variable parameter rather than as a single fixed value.

We consider an undirected weighted network  $\mathcal{G}$  with

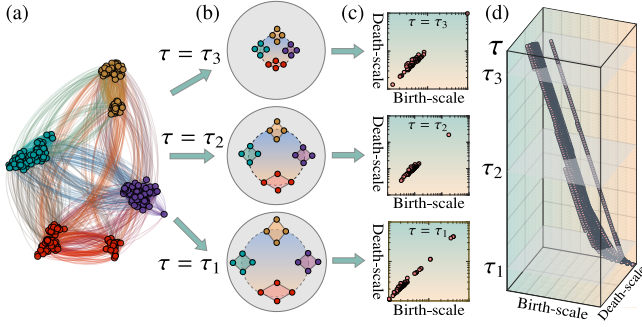


FIG. 1. (a) An undirected network comprising four clusters in which there are more connections within intra-clusters than between inter-clusters. (b) At each timescale  $\tau$ , we map the nodes to a point cloud in which the distances of the mapped points of the nodes in the same clusters are smaller than those between the nodes belonging to different clusters. These distances decrease as  $\tau$  increases as  $\tau_1 < \tau_2 < \tau_3$ . (c) The topological features at each  $\tau$  characterize the shape of the point cloud. These features are displayed as a two-dimensional persistence diagram at each  $\tau$ . (d) The scale-variant topological features, i.e. the three-dimensional persistence diagram, are obtained by integrating two-dimensional diagrams at varying  $\tau$ . The birth-scale and death-scale axes of the diagrams are represented at the logarithmic scale.

$N$  nodes  $v_1, \dots, v_N$ . We suppose that there is a single random walker, which moves randomly between nodes in continuous time. When the walker is located at  $v_i$ , we assume that the walker moves to the neighbour node  $v_j$  with the transition rate  $w_{ij}/k_i$ , where  $w_{ij} \geq 0$  represents the weight of the edge from  $v_i$  to  $v_j$  ( $i, j \in \{1, 2, \dots, N\}$ ) and  $k_i = \sum_{j=1}^N w_{ij}$ . Here,  $w_{ij} = 0$  if there is no edge between  $v_i$  and  $v_j$ . We denote  $p_{\mathcal{G},k}(\tau|i)$  as the probability of finding a random walker on  $v_k$  at time  $\tau$  that starts from  $v_i$ . The probability distribution vector  $\mathbf{p}_{\mathcal{G}}(\tau|i) = [p_{\mathcal{G},1}(\tau|i), \dots, p_{\mathcal{G},N}(\tau|i)]$ , is given according to the solution of the Kolmogorov forward equation [30]:

$$\frac{d\mathbf{p}_{\mathcal{G}}(\tau|i)}{d\tau} = -\mathbf{p}_{\mathcal{G}}(\tau|i)\mathbf{L}_{\mathcal{G}}^{\text{rw}}. \quad (1)$$

Here,  $\mathbf{L}_{\mathcal{G}}^{\text{rw}}$  is the random walk Laplacian whose components  $l_{ij}$  ( $i, j \in \{1, 2, \dots, N\}$ ) are given as  $l_{ij} = 1$  if  $i = j$  and  $k_i \neq 0$ ,  $l_{ij} = -1/k_i$  if  $i \neq j$  and  $v_i$  is adjacent to  $v_j$ , and  $l_{ij} = 0$  for otherwise.

At a specific  $\tau$ , we map the nodes of  $\mathcal{G}$  to a point cloud of  $N$  points  $\mathbf{p}_{\mathcal{G}}(\tau|1), \dots, \mathbf{p}_{\mathcal{G}}(\tau|N)$ . The shape of this point cloud provides valuable insights into the information exchange process at time  $\tau$  and the structural property of  $\mathcal{G}$  at  $\tau$ -scale. In Fig. 1(a), we consider an undirected network comprising of four clusters, in which there are more intra-cluster connections than inter-cluster connections. At each  $\tau$ , the pairwise distances of the mapped points of the nodes in the same clusters are smaller than the distances between the nodes belonging to different clusters. These distances decrease as we increase  $\tau$ . The hole patterns in the point cloud

appear with different sizes in different groups of points when  $\tau$  varies (Fig. 1(b)). Observing the formation of these holes while varying  $\tau$  can reveal the variation of topological scales for the network.

To capture the non-dyadic interactions at each  $\tau$ -scale, we construct the Vietoris-Rips simplicial complex [26, 31], which is a set of simplices built with a non-negative threshold  $\varepsilon$ . We obtain a sequence of embedded simplicial complexes called filtration with increasing  $\varepsilon$  [30]. We can highlight not only the simple connectivity but also how network properties change via the emergence and disappearance of  $l$ -dimensional holes such as connected components (zero-dimensional), loops and tunnels (one-dimensional), and voids (two-dimensional) over the filtration. We consider the emergence and disappearance of these holes as topological features for the complex network at  $\tau$ -scale. These features are visualized through multi-set points in a two-dimensional persistence diagram [26–29, 32]. In this diagram, each point  $(b, d)$  represents a hole that appears at  $\varepsilon = b$  (known as the birth-scale) and disappears at  $\varepsilon = d$  (known as the death-scale) across the filtration (Fig. 1(c)).

We obtain the scale-variant topological features that reflect the variation of the topological scales by considering the two-dimensional persistence diagrams when  $\tau$  varies. We denote  $Dg_{l,\tau}^{(2)}(\mathcal{G})$  as the two-dimensional persistence diagram of network  $\mathcal{G}$  calculated for  $l$ -dimensional holes at  $\tau$ -scale.  $Dg_{l,\tau}^{(2)}(\mathcal{G})$  can be calculated from  $\Delta_{\tau}$ , which is the distance matrix of pairwise Euclidean distances between points  $\mathbf{p}_{\mathcal{G}}(\tau|1), \dots, \mathbf{p}_{\mathcal{G}}(\tau|N)$  [30]. We consider  $\tau$  in a pre-defined set  $\mathcal{T} = \{\tau_1, \tau_2, \dots, \tau_K\}$ , where  $0 < \tau_1 < \tau_2 < \dots < \tau_K$ . We define the scale-variant topological features, i.e. the three-dimensional persistence diagram of  $l$ -dimensional holes for network  $\mathcal{G}$ , as  $Dg_l^{(3)}(\mathcal{G}) = \{(b, d, \tau) \mid (b, d) \in Dg_{l,\tau}^{(2)}(\mathcal{G}), \tau \in \mathcal{T}\}$  (Fig. 1(d)).

We show that the scale-variant topological features, i.e. the three-dimensional persistence diagrams computed from a network, are robust with respect to some perturbations of the network. To formalize such robustness, we use the bottleneck distance  $d_{B,\xi}^{(3)}$ , which is a metric structure introduced in Ref. [30, 33] for comparing three-dimensional persistence diagrams. Here,  $\xi$  is a positive rescaling coefficient introduced to adjust the scale difference between the point-wise distance and time. If two undirected networks  $\mathcal{G}$  and  $\mathcal{H}$  with the same number  $N$  of nodes are given, we can prove that the bottleneck distance between  $Dg_l^{(3)}(\mathcal{G})$  and  $Dg_l^{(3)}(\mathcal{H})$  is bounded from above by the matrix 2-norm of the difference between their random walk Laplacian matrices:

$$d_{B,\xi}^{(3)}(Dg_l^{(3)}(\mathcal{G}), Dg_l^{(3)}(\mathcal{H})) \leq 2\tau_K \|\mathbf{L}_{\mathcal{G}}^{\text{rw}} - \mathbf{L}_{\mathcal{H}}^{\text{rw}}\|_2. \quad (2)$$

Here,  $\|\mathbf{A}\|_2$  is the matrix 2-norm of matrix  $\mathbf{A}$ . In [30], we present our proof, which is based on the stability properties of two-dimensional persistence diagrams [34] and the

sensitivity of the matrix exponential [35]. The inequality of Eq. (2) indicates that our scale-variant topological features are robust with respect to the perturbation applied to the random walk Laplacian matrix. Therefore, these features can be used as discriminative features to characterize networks.

We investigate how the scale-variant topological features reflect variations of the parameters of network models. We generate networks from Girvan–Newman [36] (GN), Lancichinetti–Fortunato–Radicchi [37, 38] (LFR), Watts–Strogatz [39] (WS), Erdős–Rényi [40] (ER), Lancichinetti–Fortunato–Radicchi with hierarchical structure [17] (LFR–H) and Sales–Pardo [16] (SP) models [30]. We focus on the model parameters that represent the topological scale of these networks. These parameters are the ratio  $r$  between the probability of inter-community links ( $p_{\text{out}}$ ) and intra-community links ( $p_{\text{in}}$ ) in the GN model, the mixing rate  $\mu$  in the LFR model, the rewiring probability  $\beta$  in the WS model, the pair-link probability  $p_{\text{link}}$  in the ER model, the mixing rate  $\mu_{\text{macro}}$  for macro-communities in the LFR–H model and  $\rho$ , which quantifies the separations between topological scales in the SP model. We vary the model parameters as  $r = p_{\text{out}}/p_{\text{in}} = 0.01, 0.02, \dots, 1.0$  (GN),  $\mu = 0.01, 0.02, \dots, 1.0$  (LFR),  $\beta = 0.00, 0.01, \dots, 1.0$  (WS),  $p_{\text{link}} = 0.020, 0.021, \dots, 0.1$  (ER),  $\mu_{\text{macro}} = 0.01, 0.02, \dots, 0.2$  (LFR–H), and  $\rho = 0.05, 0.10, \dots, 2.0$  (SP). We generate 10 network realizations for each of the GN, LFR, WS, ER, and SP models, and 20 network realizations for the LFR–H model at each value of the corresponding model parameter.

We compute the three-dimensional persistence diagrams for one-dimensional holes with  $\tau_1 = 1, \tau_2 = 2, \dots, \tau_{100} = 100$ . To use the three-dimensional persistence diagrams for statistical-learning tasks, we use the positive-definite kernel mapping for such diagrams introduced in Ref. [30, 33]. Figure 2 depicts the principal components projections from the kernel space of each model, where points with different colors represent the networks generated from different values of the parameters. In WS, ER, LFR–H, and SP models, the scale-variant topological features reflect the variation of the parameters associated with the topological scales because points located at different positions have different colors (Fig. 2(c)-(f)). In GN and LFR models, there are variations in the topological scales of the network as  $r$  and  $\mu$  vary from 0 (four separate groups) to 1 (a purely random graph). We obtain the phase transition at  $r = 0.12$  and  $\mu = 0.26$  for the series of networks obtained when increasing  $r$  and  $\mu$  [30]. These values correspond to the boundaries between the identifiable phases, where parameters can be identified from the kernel space, and the non-identifiable phases (Fig. 2(a)(b)).

To evaluate the effectiveness of the scale-variant topological features, we demonstrate that the features can distinguish the networks generated from different mod-

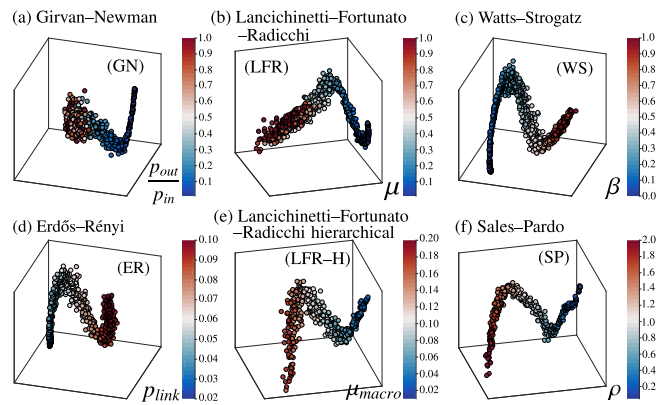


FIG. 2. Principal component projection from the kernel space of the scale-variant topological features in each considered network model. Points with different colors represent networks generated from different values of the model parameters.

els even if they have similar global statistical measures. We consider the configuration model [41], which generates random networks (known as the *configuration networks*) having the same sequences of node degrees as a given network. We label the networks generated from GN, LFR, and WS models as GN-org, LFR-org, and WS-org, respectively. The labels of their corresponding configuration networks are denoted as GN-conf, LFR-conf, and WS-conf, respectively. We perform the scale-variant method, which uses the scale-variant topological features to classify networks into these six labels. For 10 networks generated at each value of the model parameters, we randomly split them into five networks for training and the remaining five for testing. We use the support vector machine [42] for classification in the kernel space. Figure 3(a) depicts the average normalized confusion matrix over 100 random splits, where the row and column labels are predicted and true labels, respectively. Figure 3(a) shows a considerably high accuracy to identify the networks with GN-org (99.2%), LFR-org (99.2%), WS-org (99.4%), GN-conf (94.8%), LFR-conf (99.4%), and WS-conf (96.6%) labels. Using the scale-variant topological features, we can identify almost perfectly the networks that are generated from different models. Furthermore, these features can capture the difference between the networks and their configuration networks even if they have the same sequences of node degrees. This result indicates that the scale-variant topological features appear to reflect the essential behaviors of network models.

To highlight the benefits of the scale-variant method, we compare it with other conventional methods. These conventional methods use the common statistical measures extracted from the network [13, 30, 43–46], the graph kernels to measure the similarity between networks [30, 47], and the topological features calculated at an average fixed topological scale. In [30],

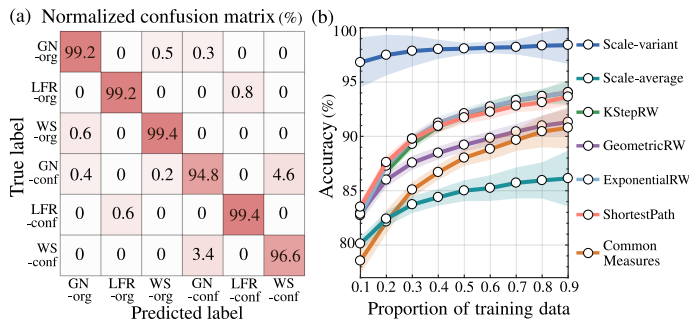


FIG. 3. We classify the networks which are generated from Girvan–Newman, Lancichinetti–Fortunato–Radicchi, and Watts–Strogatz models with labels GN-org, LFR-org, and WS-org, respectively, and their corresponding configuration networks with labels GN-conf, LFR-conf, and WS-conf, respectively. (a) The normalized confusion matrix of the scale-variant method over 100 random train-test splits of the data. For 10 networks generated at each value of the model parameters, we randomly split them into five networks for training and the remaining five for testing. (b) The average accuracies (%) of the classification methods over 100 random train-test splits at each different proportion of the training data (bold lines). The shaded areas denote the confidence interval of one standard deviations calculated from the same ensemble of runs.

we describe the graph kernels that are based on random walks (KStepRW, GeometricRW, ExponentialRW) [48, 49], paths (ShortestPath [50]), limited-sized subgraphs (Graphlet [51]) and subtree patterns (Weisfeiler–Lehman [52]). To show advantages of using variable timescales, we consider two variants of topological features calculated at an average fixed topological scale. In stead of using a specific timescale, to preserve the geometrical persistence of the point cloud, we use the scale-average and the scale-norm-average methods. The former uses the topological features extracted from the average distance matrix  $\Delta_{\text{avg}} = (1/K) \sum_{i=1}^K \Delta_{\tau_i}$ , and the latter uses the features from the average normalized distance matrix  $\hat{\Delta}_{\text{avg}} = (1/K) \sum_{i=1}^K \hat{\Delta}_{\tau_i}$  [53]. Here,  $\hat{\Delta}_{\tau_i}$  is obtained by dividing  $\Delta_{\tau_i}$  by its maximum element. For 10 networks generated at each value of the model parameters, we randomly split them with a proportion of networks for training and the remaining networks for testing. We compute the average classification accuracy over 100 random splits at different proportions of training data. Figure 3(b) depicts the performance of the methods which have the accuracies greater than 70%. Figure 3(b) highlights that the scale-variant method outperforms the other methods in terms of classification accuracy. Even with a small size of the training dataset, e.g. only 10% of all data, the scale-variant method can achieve about 97% of accuracy; in contrast, the accuracies of the other methods are not higher than 84%. Remarkably, the accuracy of the scale-variant method does not change over a wide range of proportions of training data. These re-

sults demonstrate the effectiveness and the reliability of our scale-variant method to capture the differences between network structures. The source code used in our experiments are publicly available on GitHub [54].

Next, we apply scale-variant topological features to real-world datasets of bioinformatics networks (MUTAG, BZR, COX2, DHFR, FRANKENSTEIN, PROTEINS, NCI1, NCI109) and social networks (IMDB-BINARY, IMDB-MULTI) [55–62]. We compute the three-dimensional persistence diagrams with  $\tau_1 = 1, \dots, \tau_{50} = 50$  and use the sum kernel of the normalized kernels for zero-dimensional and one-dimensional holes. Table I presents the average accuracies along with their standard deviations over 100 train-test splits. For each split of each dataset, we randomly take 80% of the networks for training and the remaining 20% for testing. In Table I, the best and the second-best average accuracy scores for each dataset are colored dark pink and light pink, respectively. The scale-variant method outperforms all the other methods on average. Further, the scale-variant method offers the best results for seven of the ten datasets and the second-best results for two more, suggesting that our method can be considered to be an effective approach for classifying real-world network data.

Finally, we use scale-variant topological features to detect transition points of the *Drosophila Melanogaster* gene regulatory network. We use a genome-wide microarray profiling that revealed the expression patterns of 4028 genes simultaneously measured during the development of *Drosophila Melanogaster* [63]. Based on Ref. [64], 66 time points are chosen from the full developmental cycle, i.e. the embryonic stage (1–30), the larval stage (31–40), the pupal stage (41–58) and the adulthood stage (59–66). The time-evolving gene regulatory networks are constructed for 588 genes, which are known to be related to the developmental process based on their gene ontologies [65]. For each network of each time point, we compute the three-dimensional persistence diagrams for one-dimensional holes with  $\tau_1 = 1, \dots, \tau_{100} = 100$ . We consider sliding windows spanning between two different stages. In each window, we compute the kernel Fisher discriminant ratio [66] for each time point from the three-dimensional persistence diagrams of networks in the window. The time point of the maximum ratio in each window is identified as the transition time point  $t_c$  [30]. From the embryonic stage to the larval stage, we obtain the transition time points as  $t_c = 28$  and  $t_c = 31$ , which are relatively close to the experimentally known transition time point  $t = 31$  from the profiling. From the larval stage to the pupal stage and from the pupal stage to the adulthood stage, we obtain the transition time points as  $t_c = 41$  and  $t_c = 59$ , respectively. These points agree with the experimentally known transition time points.

Our work is expected to become a unified analysis of complex networks. This work opens up new possibili-

TABLE I. The average and standard deviation (mean $\pm$ sd) of the classification accuracy (%) for datasets MUTAG, BZR, COX2, DHFR, FRANKENSTEIN, PROTEINS, NCI1, NCI109, IMDB-BINARY and IMDB-MULTI. In each dataset, the best and the second-best scores are colored in dark pink and light pink, respectively.

Method	MUTAG	BZR	COX2	DHFR	FRANKENSTEIN	PROTEINS	NCI1	NCI109	IMDB-BINARY	IMDB-MULTI
Scale-variant	88.3 $\pm$ 5.1	86.8 $\pm$ 3.0	78.4 $\pm$ 1.8	78.4 $\pm$ 2.9	69.4 $\pm$ 1.5	72.6 $\pm$ 2.0	71.6 $\pm$ 1.3	70.5 $\pm$ 1.2	72.9 $\pm$ 3.0	50.3 $\pm$ 2.5
Scale-average	85.9 $\pm$ 5.7	79.1 $\pm$ 1.3	77.7 $\pm$ 0.0	67.3 $\pm$ 3.1	62.7 $\pm$ 1.1	70.9 $\pm$ 1.9	66.8 $\pm$ 1.6	66.1 $\pm$ 1.6	71.0 $\pm$ 2.8	33.3 $\pm$ 0.0
Scale-norm-average	85.3 $\pm$ 6.0	81.1 $\pm$ 1.6	77.7 $\pm$ 0.0	61.2 $\pm$ 0.0	60.4 $\pm$ 1.3	71.7 $\pm$ 1.9	65.3 $\pm$ 1.8	65.6 $\pm$ 1.4	70.8 $\pm$ 2.8	46.0 $\pm$ 2.3
Graphlet	83.4 $\pm$ 5.7	78.2 $\pm$ 0.4	77.7 $\pm$ 0.0	61.2 $\pm$ 0.0	57.0 $\pm$ 0.7	71.8 $\pm$ 2.1	62.9 $\pm$ 1.5	62.8 $\pm$ 1.4	59.0 $\pm$ 3.5	41.0 $\pm$ 2.2
KStepRW	82.7 $\pm$ 5.8	85.6 $\pm$ 3.1	76.9 $\pm$ 2.0	75.7 $\pm$ 3.1	69.1 $\pm$ 1.4	73.4 $\pm$ 2.4	67.6 $\pm$ 1.5	68.1 $\pm$ 1.6	61.0 $\pm$ 3.6	45.6 $\pm$ 2.5
GeometricRW	82.8 $\pm$ 5.9	84.7 $\pm$ 3.2	77.1 $\pm$ 1.9	75.4 $\pm$ 3.0	68.8 $\pm$ 1.4	72.1 $\pm$ 2.2	65.6 $\pm$ 1.5	65.5 $\pm$ 1.5	67.5 $\pm$ 3.6	47.9 $\pm$ 2.7
ExponentialRW	82.9 $\pm$ 5.8	86.2 $\pm$ 3.2	76.9 $\pm$ 2.0	75.9 $\pm$ 3.3	68.7 $\pm$ 1.4	72.3 $\pm$ 2.3	65.4 $\pm$ 1.5	65.7 $\pm$ 1.6	66.4 $\pm$ 3.3	47.4 $\pm$ 2.6
ShortestPath	82.1 $\pm$ 6.1	84.6 $\pm$ 3.1	77.1 $\pm$ 1.7	74.7 $\pm$ 3.4	66.3 $\pm$ 1.5	72.4 $\pm$ 2.2	64.9 $\pm$ 1.5	64.7 $\pm$ 1.4	58.0 $\pm$ 3.6	43.9 $\pm$ 2.6
Weisfeiler-Lehman	85.2 $\pm$ 5.4	84.9 $\pm$ 2.8	77.4 $\pm$ 1.5	77.2 $\pm$ 3.3	71.5 $\pm$ 1.4	72.6 $\pm$ 2.2	71.0 $\pm$ 1.3	71.6 $\pm$ 1.5	61.2 $\pm$ 2.9	47.8 $\pm$ 2.3
CommonMeasures	84.7 $\pm$ 4.8	82.8 $\pm$ 1.8	77.7 $\pm$ 0.0	69.7 $\pm$ 3.0	63.7 $\pm$ 1.3	75.6 $\pm$ 2.2	67.4 $\pm$ 1.5	67.1 $\pm$ 1.4	71.6 $\pm$ 2.7	45.4 $\pm$ 2.4

ties for designing effective algorithms in network science. Such possibilities include investigation of more complicated network structures. For instance, we can employ our framework to study different aspects of multiplex networks or apply it to the structural reducibility of a multi-layer network while preserving its dynamics and function.

\* zoro@biom.t.u-tokyo.ac.jp

† tuan@biom.t.u-tokyo.ac.jp

‡ hasegawa@biom.t.u-tokyo.ac.jp

- [1] D. Taylor, F. Klimm, H. A. Harrington, M. Kramár, K. Mischaikow, M. A. Porter, and P. J. Mucha, *Nat. Commun.* **6**, 7723 (2015).
- [2] J. G. T. Zañudo, G. Yang, and R. Albert, *Proc. Natl Acad. Sci. USA* **114**, 7234 (2017).
- [3] M. Santolini and A.-L. Barabási, *Proc. Natl Acad. Sci. USA* **115**, E6375 (2018).
- [4] K. Sun, J. P. Gonçalves, C. Larminie, and N. Pržulj, *BMC Bioinformatics* **15**, 304 (2014).
- [5] A. Calderone, M. Formenti, F. Aprea, M. Papa, L. Alberghina, A. M. Colangelo, and P. Bertolazzi, *BMC Syst. Biol.* **10**, 25 (2016).
- [6] T. A. Schieber, L. Carpi, A. Díaz-Guilera, P. M. Pardalos, C. Masoller, and M. G. Ravetti, *Nat. Commun.* **8**, 13928 (2017).
- [7] L. Carpi, P. Saco, O. Rosso, and M. Ravetti, *Eur. Phys. J. B* **85**, 389 (2012).
- [8] I. Barnett and J.-P. Onnela, *Sci. Rep.* **6**, 18893 (2016).
- [9] W. Bao and G. Michailidis, *Sci. Rep.* **8**, 12938 (2018).
- [10] Y.-Y. Ahn, J. P. Bagrow, and S. Lehmann, *Nature* **466**, 761 (2010).
- [11] R. F. Betzel and D. S. Bassett, *Neuroimage* **160**, 73 (2017).
- [12] R. E. Boulos, N. Tremblay, A. Arneodo, P. Borgnat, and B. Audit, *BMC Bioinformatics* **18**, 209 (2017).
- [13] L. d. F. Costa, F. A. Rodrigues, G. Travieso, and P. R. Villas Boas, *Adv. Phys.* **56**, 167 (2007).
- [14] M. E. J. Newman, *Networks: An Introduction* (Oxford Univ. Press, 2010).
- [15] A. Arenas, A. Díaz-Guilera, and C. J. Pérez-Vicente, *Phys. Rev. Lett.* **96**, 114102 (2006).
- [16] M. Sales-Pardo, R. Guimera, A. A. Moreira, and L. A. N. Amaral, *Proc. Natl Acad. Sci. USA* **104**, 15224 (2007).
- [17] A. Lancichinetti, S. Fortunato, and J. Kertész, *New J. Phys.* **11**, 033015 (2009).
- [18] N. Tremblay and P. Borgnat, *IEEE Trans. Signal Process.* **62**, 5227 (2014).
- [19] S. A. Marvel, J. Kleinberg, R. D. Kleinberg, and S. H. Strogatz, *Proc. Natl Acad. Sci. USA* **108**, 1771 (2011).
- [20] A. van der Schaft, S. Rao, and B. Jayawardhana, *SIAM J. Appl. Math.* **73**, 953 (2013).
- [21] M. W. Reimann, M. Nolte, M. Scolamiero, K. Turner, R. Perin, G. Chindemi, P. Dotko, R. Levi, K. Hess, and H. Markram, *Frontiers in Computational Neuroscience* **11**, 48 (2017).
- [22] M. A. de Menezes and A.-L. Barabási, *Phys. Rev. Lett.* **92**, 028701 (2004).
- [23] D. K. Wells, W. L. Kath, and A. E. Motter, *Phys. Rev. X* **5**, 031036 (2015).
- [24] J. Hindes and I. B. Schwartz, *Phys. Rev. Lett.* **117**, 028302 (2016).
- [25] A.-L. Barabási *et al.*, *Network science* (Cambridge Univ. Press, 2016).
- [26] H. Edelsbrunner and J. Harer, *Computational Topology: An Introduction* (Amer. Math. Soc., 2010).
- [27] H. Edelsbrunner, D. Letscher, and A. Zomorodian, *Discrete Comput. Geom.* **28**, 511 (2002).
- [28] A. Zomorodian and G. Carlsson, *Discrete Comput. Geom.* **33**, 249 (2005).
- [29] G. Carlsson, *Bull. Amer. Math. Soc.* **46**, 255 (2009).
- [30] See Supplemental Material.
- [31] T. Kaczynski, K. Mischaikow, and M. Mrozek, *Computational homology*, Vol. 157 (Springer, 2006).
- [32] K. Mischaikow and V. Nanda, *Discrete Comput. Geom.* **50**, 330 (2013).
- [33] Q. H. Tran and Y. Hasegawa, Preprint at arXiv:1803.00208.
- [34] F. Chazal, V. de Silva, and S. Oudot, *Geometriae Dedicata* **173**, 193 (2014).
- [35] G. H. Golub and C. F. Van Loan, *Matrix computations*, Vol. 3 (JHU Press, 2012).
- [36] M. E. J. Newman and M. Girvan, *Phys. Rev. E* **69**, 026113 (2004).
- [37] A. Lancichinetti, S. Fortunato, and F. Radicchi, *Phys. Rev. E* **78**, 046110 (2008).
- [38] A. Lancichinetti and S. Fortunato, *Phys. Rev. E* **80**,

- 016118 (2009).
- [39] D. J. Watts and S. H. Strogatz, *Nature* **393**, 440 (1998).
- [40] P. Erdős and A. Rényi, *Publ. Math.* **6**, 290 (1959).
- [41] M. E. J. Newman, S. H. Strogatz, and D. J. Watts, *Phys. Rev. E* **64**, 026118 (2001).
- [42] C. M. Bishop, *Pattern Recognition and Machine Learning* (Springer, 2006).
- [43] L. C. Freeman, *Soc. Networks* **1**, 215 (1978).
- [44] V. Latora and M. Marchiori, *Phys. Rev. Lett.* **87**, 198701 (2001).
- [45] M. E. J. Newman, *Phys. Rev. Lett.* **89**, 208701 (2002).
- [46] U. Brandes, *Soc. Networks* **30**, 136 (2008).
- [47] M. Sugiyama, M. E. Ghisu, F. Llinares-López, and K. Borgwardt, *Bioinformatics* **34**, 530 (2017).
- [48] H. Kashima, K. Tsuda, and A. Inokuchi, in *Proc. 20th Int. Conf. Machine Learning (ICML)* (2003) pp. 321–328.
- [49] T. Gärtner, P. Flach, and S. Wrobel, in *Proc. 16th Annual Conf. Computational Learning Theory* (2003) pp. 129–143.
- [50] K. M. Borgwardt and H.-P. Kriegel, in *Proc. 5th IEEE Int. Conf. Data Mining (ICDM)* (2005) pp. 74–81.
- [51] K. M. Borgwardt, T. Petri, S. Vishwanathan, and H.-P. Kriegel, in *Proc. Mining and Learning with Graphs (MLG)* (2007).
- [52] N. Shervashidze, P. Schweitzer, E. J. v. Leeuwen, K. Mehlhorn, and K. M. Borgwardt, *JMLR* **12**, 2539 (2011).
- [53] M. De Domenico, *Phys. Rev. Lett.* **118**, 168301 (2017).
- [54] Q. H. Tran, V. T. Vo, and Y. Hasegawa, “Scale-variant topological information,” <https://github.com/OminiaVincit/scale-variant-topo>, GitHub Repository.
- [55] A. K. Debnath, R. L. Lopez de Compadre, G. Debnath, A. J. Shusterman, and C. Hansch, *J. Med. Chem.* **34**, 786 (1991).
- [56] J. J. Sutherland, L. A. O’Brien, and D. F. Weaver, *J. Chem. Inf. Comput. Sci.* **43**, 1906 (2003).
- [57] J. Kazius, R. McGuire, and R. Bursi, *J. Med. Chem.* **48**, 312 (2005).
- [58] K. M. Borgwardt, C. S. Ong, S. Schönauer, S. Vishwanathan, A. J. Smola, and H.-P. Kriegel, *Bioinformatics* **21**, i47 (2005).
- [59] N. Wale, I. A. Watson, and G. Karypis, *Knowledge and Information Systems* **14**, 347 (2008).
- [60] F. Orsini, P. Frasconi, and L. De Raedt, in *Proc. 24th Int. Joint Conf. Artificial Intelligence (IJCAI)* (2015) pp. 3756–3762.
- [61] P. Yanardag and S. Vishwanathan, in *Proc. 21th ACM SIGKDD Int. Conf. Knowledge Discovery and Data Mining (KDD)* (2015) pp. 1365–1374.
- [62] K. Kersting, N. M. Kriege, C. Morris, P. Mutzel, and M. Neumann, “Benchmark data sets for graph kernels,” (2016), <http://graphkernels.cs.tu-dortmund.de>.
- [63] M. N. Arbeitman, E. E. Furlong, F. Imam, E. Johnson, B. H. Null, B. S. Baker, M. A. Krasnow, M. P. Scott, R. W. Davis, and K. P. White, *Science* **297**, 2270 (2002).
- [64] J. Zhang and J. Cao, *J. Am. Stat. Assoc.* **112**, 994 (2017).
- [65] L. Song, M. Kolar, and E. P. Xing, *Bioinformatics* **25**, i128 (2009).
- [66] Z. Harchaoui, E. Moulines, and F. R. Bach, in *Adv. Neural Inf. Process. Syst. 21 (NIPS)* (2009) pp. 609–616.

# Supplemental Material for “Scale-variant Topological Information for Characterizing Complex Networks”

Quoc Hoan Tran, Van Tuan Vo and Yoshihiko Hasegawa

This supplementary material describes in detail the calculations introduced in the main text and additional figures. Equation, figure and table numbers in this section are prefixed with S (e.g., Eq. (S1) or Fig. S1, Table S1). Numbers without the prefix (e.g., Eq. (1) or Fig. 1, Table 1) refer to items in the main text.

## 1 Construction of Vietoris–Rips filtration of a network

In the following sections, we define and describe in Fig. S1 the process of extracting topological features of a complex network at each specific timescale  $\tau$ .

We consider an undirected weighted network  $\mathcal{G}$  with  $N$  nodes  $v_1, \dots, v_N$ . We denote  $\mathbf{L}_{\mathcal{G}}^{\text{rw}}$  as the random walk Laplacian of network  $\mathcal{G}$ . At a specific  $\tau$ , we map the nodes of network  $\mathcal{G}$  to a point cloud of  $N$  points  $\mathbf{p}_{\mathcal{G}}(\tau|1), \dots, \mathbf{p}_{\mathcal{G}}(\tau|N)$ . Here,  $\mathbf{p}_{\mathcal{G}}(\tau|i)$  is given according to the solution of the Kolmogorov forward equation:

$$\frac{d\mathbf{p}_{\mathcal{G}}(\tau|i)}{d\tau} = -\mathbf{p}_{\mathcal{G}}(\tau|i)\mathbf{L}_{\mathcal{G}}^{\text{rw}}. \quad (\text{S1})$$

The solution for Eq. (S1) is  $\mathbf{p}_{\mathcal{G}}(\tau|i) = \mathbf{u}_i \exp(-\tau\mathbf{L}_{\mathcal{G}}^{\text{rw}})$ , where  $\mathbf{u}_i = [0, \dots, 0, 1, 0, \dots, 0]$  with its  $i$ -th element being equal to 1; others are equal to 0.

At each  $\tau$ , we calculate the diffusion distance matrix  $\Delta_{\tau}$  of size  $N \times N$ , whose element  $\Delta_{ij}$  is the Euclidean distance between points  $\mathbf{p}_{\mathcal{G}}(\tau|i)$  and  $\mathbf{p}_{\mathcal{G}}(\tau|j)$  (Fig. S1(a)). If  $\varepsilon = 0$ , the nodes of the network can be considered discrete points. As we increase  $\varepsilon$ , new pairwise connections and simplices may appear when  $\varepsilon$  meets each value of  $\Delta_{ij}$ . We obtain a filtration as a sequence of embedded simplicial complexes. Hole patterns such as connected components or loops can appear or disappear over this filtration. For instance, in Fig. S1(b), at  $\varepsilon = 0$ , we have six separated nodes considered as six separated connected components, but at  $\varepsilon = 0.407$ , three nodes are connected with each other; thus, two connected components disappear at this scale. We can describe these patterns as two blue bars started at scale 0 and ended at scale 0.407. The same explanation with the red bar started at scale 0.428 and ended at scale 0.430, which represents the emergence of loop pattern ( $v_1 \rightarrow v_2 \rightarrow v_3 \rightarrow v_5 \rightarrow v_1$ ) at  $\varepsilon = 0.428$  and the disappearance at  $\varepsilon = 0.430$ . Figure S1(c) illustrates the corresponding persistence diagrams for zero-dimensional holes and one-dimensional holes, where the birth-scale and the death-scale are represented for the values of  $\varepsilon$  at the emergence and the disappearance of the holes.

arXiv:1811.03573v3 [cs.SI] 10 Jan 2019

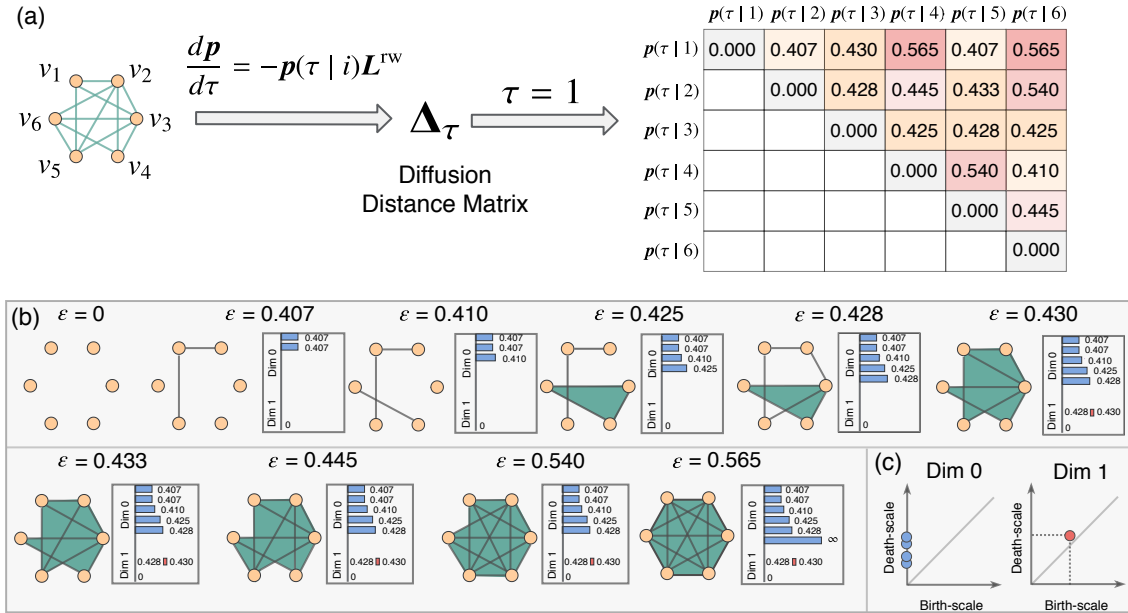


FIG. S1. **Construction of Vietoris–Rips filtration of a complex network at a specific timescale  $\tau$ .** We map nodes  $v_1, \dots, v_N$  of the network to a point cloud of  $N$  points  $\mathbf{p}(\tau|1), \dots, \mathbf{p}(\tau|N)$  through a diffusion dynamics described by the random walk Laplacian  $L^{\text{rw}}$ . (a) Diffusion distance matrix  $\Delta_\tau$  of size  $N \times N$ , whose element  $\Delta_{ij}$  is the Euclidean distance between points  $\mathbf{p}(\tau|i)$  and  $\mathbf{p}(\tau|j)$ . (b) A complex is built over a set of points if the pairwise distances between them are less than or equal to a distance-scale parameter  $\varepsilon$ . If  $\varepsilon = 0$ , we have the discrete points. As  $\varepsilon$  takes the increasing sequence values of diffusion distance  $\Delta_{ij}$ , the hole patterns such as connected components (zero-dimensional hole) or loops (one-dimensional hole) can appear or disappear over this filtration. The lifetime of these hole patterns are described as blue bars (for zero-dimensional holes) and red bars (for one-dimensional holes). These bars begin at the values of  $\varepsilon$  when the holes appear, then end at values when the holes disappear. (c) The corresponding persistence diagrams for zero-dimensional and one-dimensional holes. The birth-scale and the death-scale are represented for the values of  $\varepsilon$  at the emergence and the disappearance of the holes.

## 2 Stability of scale-variant topological features

To prove the stability property of the topological features undergoing network perturbation, we introduce the concept of the bottleneck distance between two two-dimensional diagrams first. Let  $X$  and  $Y$  be finite sets of points embedded in the Euclidean space  $\mathbb{R}^n$ . Denote their *two*-dimensional persistent diagrams for  $l$ -dimensional holes as  $DgX$  and  $DgY$ , respectively. We consider all matchings,  $\gamma$ , such that a point on one diagram is matched to a point on the other diagram or to its projection on the line  $b = d$  in two-dimensional space. The bottleneck distance  $d_B^{(2)}$  between  $DgX$  and  $DgY$  is defined as the infimum of the longest matched infinity-norm distance over all matchings,  $\gamma$ :

$$d_B^{(2)}(DgX, DgY) = \inf_{\gamma} \max_{(\mathbf{p}, \mathbf{q}) \in \gamma} \|\mathbf{p} - \mathbf{q}\|_{\infty}. \quad (\text{S2})$$

The bottleneck distance between the two-dimensional persistence diagrams satisfies the following inequality [6]:

$$d_B^{(2)}(DgX, DgY) \leq 2d_H(X, Y), \quad (\text{S3})$$

where  $d_H(X, Y)$  is the Hausdorff distance given as

$$d_H(X, Y) = \max \left\{ \max_{\mathbf{x} \in X} \min_{\mathbf{y} \in Y} d(\mathbf{x}, \mathbf{y}), \max_{\mathbf{y} \in Y} \min_{\mathbf{x} \in X} d(\mathbf{x}, \mathbf{y}) \right\}. \quad (\text{S4})$$

Here,  $d(\mathbf{x}, \mathbf{y})$  is the Euclidean distance between two points  $\mathbf{x}, \mathbf{y}$  in  $\mathbb{R}^n$ .

Given two three-dimensional persistence diagrams as  $E$  and  $F$ , consider all matchings  $\psi$  such that a point on one diagram is matched to a point on the other diagram or to its projection on the plane  $b = d$ . For each pair  $(\mathbf{p}, \mathbf{q}) \in \psi$  for which  $\mathbf{p} = (b_1, d_1, \tau_1)$  and  $\mathbf{q} = (b_2, d_2, \tau_2)$ , we define *the relative infinity-norm distance* between  $\mathbf{p}$  and  $\mathbf{q}$  as  $d_{\xi}^{(\infty)}(\mathbf{p}, \mathbf{q}) = \max(|b_1 - b_2|, |d_1 - d_2|, \xi|\tau_1 - \tau_2|)$ , where  $\xi$  is a positive rescaling coefficient introduced to adjust the scale difference between the point-wise distance and time. The bottleneck distance,  $d_{B, \xi}^{(3)}(E, F)$ , is defined as the infimum of the longest matched relative infinity-norm distance over all matchings  $\psi$ :

$$d_{B, \xi}^{(3)}(E, F) = \inf_{\psi} \max_{(\mathbf{p}, \mathbf{q}) \in \psi} d_{\xi}^{(\infty)}(\mathbf{p}, \mathbf{q}). \quad (\text{S5})$$

For each  $\tau \in \mathcal{T}$  and two networks  $\mathcal{G}, \mathcal{H}$  with the same number  $N$  of nodes, we first prove the following inequality:

$$d_B^{(2)}(Dg_{l, \tau}^{(2)}(\mathcal{G}), Dg_{l, \tau}^{(2)}(\mathcal{H})) \leq 2\tau \|\mathbf{L}_{\mathcal{G}}^{\text{rw}} - \mathbf{L}_{\mathcal{H}}^{\text{rw}}\|_2. \quad (\text{S6})$$

Here, two two-dimensional persistence diagrams  $Dg_{l, \tau}^{(2)}(\mathcal{G})$  and  $Dg_{l, \tau}^{(2)}(\mathcal{H})$  are calculated for  $l$ -dimensional holes from two point clouds  $\mathbf{P}_{\mathcal{G}, \tau} = \{\mathbf{p}_{\mathcal{G}}(\tau|1), \dots, \mathbf{p}_{\mathcal{G}}(\tau|N)\}$  and  $\mathbf{P}_{\mathcal{H}, \tau} = \{\mathbf{p}_{\mathcal{H}}(\tau|1), \dots, \mathbf{p}_{\mathcal{H}}(\tau|N)\}$ , respectively.

By applying Eq. (S3) with  $\mathbf{P}_{\mathcal{G}, \tau}$  and  $\mathbf{P}_{\mathcal{H}, \tau}$ , we have

$$d_B^{(2)}(Dg_{l, \tau}^{(2)}(\mathcal{G}), Dg_{l, \tau}^{(2)}(\mathcal{H})) \leq 2d_H(\mathbf{P}_{\mathcal{G}, \tau}, \mathbf{P}_{\mathcal{H}, \tau}), \quad (\text{S7})$$

From the definition of the Hausdorff distance, we have

$$d_H(\mathbf{P}_{\mathcal{G}, \tau}, \mathbf{P}_{\mathcal{H}, \tau}) = \max \left\{ \max_i \min_j d(\mathbf{p}_{\mathcal{G}}(\tau|i), \mathbf{p}_{\mathcal{H}}(\tau|j)), \max_j \min_i d(\mathbf{p}_{\mathcal{G}}(\tau|i), \mathbf{p}_{\mathcal{H}}(\tau|j)) \right\} \quad (\text{S8})$$

$$\leq \max \left\{ \max_i d(\mathbf{p}_{\mathcal{G}}(\tau|i), \mathbf{p}_{\mathcal{H}}(\tau|i)), \max_j d(\mathbf{p}_{\mathcal{G}}(\tau|j), \mathbf{p}_{\mathcal{H}}(\tau|j)) \right\} \quad (\text{S9})$$

$$= \max_i d(\mathbf{p}_{\mathcal{G}}(\tau|i), \mathbf{p}_{\mathcal{H}}(\tau|i)). \quad (\text{S10})$$

Since  $\mathbf{p}_{\mathcal{G}}(\tau|i) = \mathbf{u}_i \exp(-\tau \mathbf{L}_{\mathcal{G}}^{\text{rw}})$  and  $\mathbf{p}_{\mathcal{H}}(\tau|i) = \mathbf{u}_i \exp(-\tau \mathbf{L}_{\mathcal{H}}^{\text{rw}})$ , we have

$$d(\mathbf{p}_{\mathcal{G}}(\tau|i), \mathbf{p}_{\mathcal{H}}(\tau|i)) = \|\mathbf{u}_i (e^{-\tau \mathbf{L}_{\mathcal{G}}^{\text{rw}}} - e^{-\tau \mathbf{L}_{\mathcal{H}}^{\text{rw}}})\|_2 \quad (\text{S11})$$

$$\leq \|\mathbf{u}_i\|_2 \|e^{-\tau \mathbf{L}_{\mathcal{G}}^{\text{rw}}} - e^{-\tau \mathbf{L}_{\mathcal{H}}^{\text{rw}}}\|_2 = \|e^{-\tau \mathbf{L}_{\mathcal{G}}^{\text{rw}}} - e^{-\tau \mathbf{L}_{\mathcal{H}}^{\text{rw}}}\|_2. \quad (\text{S12})$$

We write the difference of the matrix exponential in terms of an integral [12],

$$\|e^{-\tau \mathbf{L}_{\mathcal{G}}^{\text{rw}}} - e^{-\tau \mathbf{L}_{\mathcal{H}}^{\text{rw}}}\|_2 = \left\| \int_0^{\tau} e^{-\mathbf{L}_{\mathcal{G}}^{\text{rw}}(\tau-t)} \mathbf{E} e^{-\mathbf{L}_{\mathcal{H}}^{\text{rw}}t} dt \right\|_2 \quad (\text{S13})$$

$$\leq \int_0^{\tau} \|e^{-\mathbf{L}_{\mathcal{G}}^{\text{rw}}(\tau-t)} \mathbf{E} e^{-\mathbf{L}_{\mathcal{H}}^{\text{rw}}t}\|_2 dt \leq \|\mathbf{E}\|_2 \int_0^{\tau} \|e^{-\mathbf{L}_{\mathcal{G}}^{\text{rw}}(\tau-t)}\|_2 \|e^{-\mathbf{L}_{\mathcal{H}}^{\text{rw}}t}\|_2 dt, \quad (\text{S14})$$

where  $\mathbf{E} = \mathbf{L}_G^{\text{rw}} - \mathbf{L}_H^{\text{rw}}$ . We know that  $-\mathbf{L}_G^{\text{rw}}$  is a negative semi-definite matrix with the largest eigenvalue equal to 0. It implies that the largest eigenvalue of  $e^{-\mathbf{L}_G^{\text{rw}}(\tau-t)}$  is equal to 1, and hence  $\|e^{-\mathbf{L}_G^{\text{rw}}(\tau-t)}\|_2 = 1$ . We obtain the same result with  $-\mathbf{L}_H^{\text{rw}}$ , i.e.  $\|e^{-\mathbf{L}_H^{\text{rw}}t}\|_2 = 1$ . Then, from Eq. (S12) and Eq. (S14), we have

$$d(\mathbf{p}_G(\tau|i), \mathbf{p}_H(\tau|i)) \leq \|\mathbf{E}\|_2 \int_0^\tau 1 dt = \tau \|\mathbf{E}\|_2 = \tau \|\mathbf{L}_G^{\text{rw}} - \mathbf{L}_H^{\text{rw}}\|_2. \quad (\text{S15})$$

From Eq. (S7), Eq. (S10) and Eq. (S15), we have the result in Eq. (S6).

Let  $\Gamma_\tau$  be the set of matchings defined in Eq. (S2) between two two-dimensional persistence diagrams  $Dg_{l,\tau}^{(2)}(\mathcal{G})$  and  $Dg_{l,\tau}^{(2)}(\mathcal{H})$ . For each collection  $\Lambda = \{\gamma_1, \gamma_2, \dots, \gamma_K \mid \gamma_i \in \Gamma_\tau, i = 1, 2, \dots, K\}$ , we construct the matching  $\psi$  between two three-dimensional persistence diagrams  $Dg_l^{(3)}(\mathcal{G})$  and  $Dg_l^{(3)}(\mathcal{H})$ , such that, for each  $(\mathbf{p}, \mathbf{q}) \in \psi$ , then  $\mathbf{p} = (b_1, d_1, \tau)$ ,  $\mathbf{q} = (b_2, d_2, \tau)$ , and  $(\mathbf{p}_\gamma, \mathbf{q}_\gamma) \in \gamma$ , where  $\mathbf{p}_\gamma = (b_1, d_1)$ ,  $\mathbf{q}_\gamma = (b_2, d_2)$  and  $\gamma \in \Lambda \cap \Gamma_\tau$ . Let  $\Gamma$  be a set of all matchings  $\psi$  constructed this way. From the definition of the bottleneck distance, we have the following inequality:

$$d_{B,\xi}^{(3)}(Dg_l^{(3)}(\mathcal{G}), Dg_l^{(3)}(\mathcal{H})) \leq \inf_{\psi \in \Gamma} \max_{(\mathbf{p}, \mathbf{q}) \in \psi} d_\xi^{(\infty)}(\mathbf{p}, \mathbf{q}). \quad (\text{S16})$$

For  $(\mathbf{p}, \mathbf{q}) \in \psi$ , we have

$$d_\xi^{(\infty)}(\mathbf{p}, \mathbf{q}) = \max\{|b_1 - b_2|, |d_1 - d_2|, \xi|\tau - \tau|\} \quad (\text{S17})$$

$$= \max\{|b_1 - b_2|, |d_1 - d_2|\} = \|\mathbf{p}_\gamma - \mathbf{q}_\gamma\|_\infty, \quad (\text{S18})$$

and Eq. (S16) becomes

$$d_{B,\xi}^{(3)}(Dg_l^{(3)}(\mathcal{G}), Dg_l^{(3)}(\mathcal{H})) \leq \max_{\tau \in \mathcal{T}} \inf_{\gamma \in \Gamma_\tau} \max_{(\mathbf{p}_\gamma, \mathbf{q}_\gamma) \in \gamma} \|\mathbf{p}_\gamma - \mathbf{q}_\gamma\|_\infty \quad (\text{S19})$$

$$= \max_{\tau \in \mathcal{T}} d_B^{(2)}(Dg_{l,\tau}^{(2)}(\mathcal{G}), Dg_{l,\tau}^{(2)}(\mathcal{H})). \quad (\text{S20})$$

From Eq. (S6) and Eq. (S20), we obtain Eq. (2) in the main text, which is the stability property of our scale-variant features.

### 3 Kernel method for three-dimensional persistence diagrams

Given the positive bandwidth  $\sigma$  and the positive rescaling coefficient  $\xi$  introduced to adjust the scale difference between the point-wise distance and time, we define the kernel  $k_{\sigma,\xi}$  between two three-dimensional persistence diagrams,  $E$  and  $F$ , as

$$k_{\sigma,\xi}(E, F) = \frac{1}{\sigma\sqrt{2\pi}} \sum_{\mathbf{p} \in E, \mathbf{q} \in F} \left( e^{-\frac{d_\xi^2(\mathbf{p}, \mathbf{q})}{2\sigma^2}} - e^{-\frac{d_\xi^2(\mathbf{p}, \bar{\mathbf{q}})}{2\sigma^2}} \right), \quad (\text{S21})$$

where  $d_\xi^2(\mathbf{p}, \mathbf{q}) = |b_1 - b_2|^2 + |d_1 - d_2|^2 + \xi^2|\tau_1 - \tau_2|^2$ ,  $d_\xi^2(\mathbf{p}, \bar{\mathbf{q}}) = |b_1 - d_2|^2 + |d_1 - b_2|^2 + \xi^2|\tau_1 - \tau_2|^2$ , with  $\mathbf{p} = (b_1, d_1, \tau_1)$  and  $\mathbf{q} = (b_2, d_2, \tau_2)$ ,  $\bar{\mathbf{q}} = (d_2, b_2, \tau_2)$ . In our experiments, we use the normalized version of the kernel, which is calculated as

$$k_{\sigma,\xi}(E, F) \leftarrow k_{\sigma,\xi}(E, F) / \sqrt{k_{\sigma,\xi}(E, E)k_{\sigma,\xi}(F, F)}, \quad (\text{S22})$$

where  $E, F$  are two persistence diagrams.

We set the rescale coefficient to  $\xi = \sigma$  and present here a heuristic method to select the bandwidth  $\sigma$ . Given the kernel values calculated from the three-dimensional persistence diagrams  $Dg_1^{(3)}, Dg_2^{(3)}, \dots, Dg_M^{(3)}$ , we denote  $\sigma_s^2 = \text{median}\{(b_i - b_j)^2 + (d_i - d_j)^2 \mid (b_i, d_i, \tau_i), (b_j, d_j, \tau_j) \in Dg_s^{(3)}\}$  with  $s = 1, 2, \dots, M$ . We set  $\sigma$  as  $\sigma^2 = \frac{1}{2} \text{median}\{\sigma_s^2 \mid s = 1, \dots, N\}$  such that  $2\sigma^2$  takes values close to many  $(b_i - b_j)^2 + (d_i - d_j)^2$  values.

### 4 Kernel Fisher discriminant ratio

The kernel method maps persistence diagrams in an abstract space, namely, a reproducing Hilbert space  $\mathcal{H}$  associated with a reproducing kernel  $k(\cdot, \cdot)$  and a feature map  $\Phi(DgX) = k(DgX, \cdot)$ . The inner product between two operators  $\Phi(DgX)$  and  $\Phi(DgY)$  is defined as  $\langle \Phi(DgX), \Phi(DgY) \rangle_{\mathcal{H}} = k(DgX, DgY)$ . Here,

$DgX$  and  $DgY$  are two three-dimensional persistence diagrams. We consider a collection of diagrams  $\mathcal{D} = \{Dg_1, \dots, Dg_M\}$  and a given index  $s > 1$ . The kernel Fisher discriminant ratio  $\text{KFDR}_{M,s}(\mathcal{D})$  is a statistical quantity to measure the dissimilarity between two classes assumptively defined by two sets of diagrams having index before and from  $s$  [13]. Here, the index  $s$  achieving the maximum of  $\text{KFDR}_{M,s}(\mathcal{D})$  corresponds to the estimated transition point.

The corresponding empirical mean elements and covariance operators associated with the data in  $\mathcal{D}$  having index before and from  $s$  are defined as

$$\hat{\mu}_1 = \frac{1}{s-1} \sum_{i=1}^{s-1} k(Dg_i, \cdot), \quad (\text{S23})$$

$$\hat{\Sigma}_1 = \frac{1}{s-1} \sum_{i=1}^{s-1} \{k(Dg_i, \cdot) - \hat{\mu}_1\} \otimes \{k(Dg_i, \cdot) - \hat{\mu}_1\}, \quad (\text{S24})$$

$$\hat{\mu}_2 = \frac{1}{M-s+1} \sum_{i=s}^M k(Dg_i, \cdot), \quad (\text{S25})$$

$$\hat{\Sigma}_2 = \frac{1}{M-s+1} \sum_{i=s}^M \{k(Dg_i, \cdot) - \hat{\mu}_2\} \otimes \{k(Dg_i, \cdot) - \hat{\mu}_2\}. \quad (\text{S26})$$

Here,  $f \otimes g$  for two operators  $f, g \in \mathcal{H}$  is defined for all operators  $h \in \mathcal{H}$  as  $(f \otimes g)h = \langle g, h \rangle_{\mathcal{H}} f$ .

The kernel Fisher discriminant ratio  $\text{KFDR}_{M,s}(\mathcal{D})$  is defined as

$$\text{KFDR}_{M,s}(\mathcal{D}) = \frac{(s-1)(M-s+1)}{M} \left\langle \hat{\mu}_2 - \hat{\mu}_1, (\hat{\Sigma} + \gamma \mathbf{I})^{-1} (\hat{\mu}_2 - \hat{\mu}_1) \right\rangle_{\mathcal{H}}, \quad (\text{S27})$$

where  $\gamma$  is a regularization parameter and  $\hat{\Sigma} = \frac{s-1}{M} \hat{\Sigma}_1 + \frac{M-s+1}{M} \hat{\Sigma}_2$ .

We set  $\gamma = 10^{-1}, 10^{-1}, 10^{-5}$  in the experiments of the Girvan–Newman (GN) network, Lancichinetti–Fortunato–Radicchi (LFR) network and *Drosophila Melanogaster* network, respectively.

## 5 Network models

We describe network models used in our experiments.

### 5.1 Girvan–Newman (GN) model

Girvan–Newman model is a particular case of the planted  $l$ -partition model [22]. We use the network with 128 nodes partitioned into four communities of size 32 and the average degree of 16. In the Girvan–Newman model, we focus on the ratio  $r$  between the probability of inter-community links ( $p_{\text{out}}$ ) and intra-community links ( $p_{\text{in}}$ ). We vary  $r = p_{\text{out}}/p_{\text{in}} = 0.01, 0.02, \dots, 1.0$  and generate 10 random realizations of the network for each value of  $r$ .

### 5.2 Lancichinetti–Fortunato–Radicchi (LFR) model

Lancichinetti–Fortunato–Radicchi is a model that generates a network with a priority known communities, and both the node degrees and the community size follow the power-law distribution [19, 17]. We focus on the mixing rate  $\mu$  ( $0 \leq \mu \leq 1.0$ ), where each node shares a fraction  $1 - \mu$  of links with the nodes inside its community and a fraction of  $\mu$  with the nodes outside its community. For the standard Lancichinetti–Fortunato–Radicchi model, we set the number of nodes as 128, the average and the maximum degrees as 16 and 32 and the minimum and the maximum community sizes as 16 and 32, respectively. The power-law exponent coefficients for the degree distribution, the community size distribution and the weights distribution are  $t_1 = -2, t_2 = -1$  and  $t_3 = 1$ , respectively. We vary the mixing rate as  $\mu = 0.01, 0.2, \dots, 1.0$  and use the program provided by Ref. [19] to generate 10 random realizations of a network for each value of  $\mu$ .

### 5.3 Watts–Strogatz (WS) model

Watts–Strogatz model is a model that generates random networks with the small-world properties by rewiring links in a circle in which only neighbors are connected initially [31]. We generate networks from the Watts–Strogatz model with 128 nodes and rewiring probability  $\beta = 0.00, 0.01, \dots, 1.0$ , with 10 random realizations for each value of  $\beta$ .

## 5.4 Erdős–Rényi (ER) model

The Erdős–Rényi model is a classical model that generates random networks [9]. We set the number of nodes as 128, vary the pair-link probability  $p_{\text{link}} = 0.020, 0.021, \dots, 0.1$  and generate 10 random realizations of the networks for each value of  $p_{\text{link}}$ .

## 5.5 Lancichinetti–Fortunato–Radicchi with hierarchical structure (LFR–H) model

We generate networks from the hierarchical structure version of Lancichinetti–Fortunato–Radicchi model with the hierarchical structure of communities [18]. The number of nodes is 300, the minimum and the maximum sizes of the micro-community are 10 and 50, the minimum and the maximum sizes of the macro-community are 20 and 80 and the average and the maximum degrees are 20 and 25, respectively. The power-law exponent coefficients for the degree distribution, the community size distribution and the weights distribution are the same as for the standard Lancichinetti–Fortunato–Radicchi model. We keep the mixing rate for the micro-communities as  $\mu_{\text{micro}} = 0.16$ , and vary the mixing value for the macro-communities as  $\mu_{\text{macro}} = 0.01, 0.02, \dots, 0.2$  with 20 random realizations for each value of  $\mu_{\text{macro}}$ .

## 5.6 Sales–Pardo (SP) model

Sales–Pardo model is a model that generates hierarchical networks with 640 nodes and three community structures nested in one another [24]. There are 64 communities of 10 nodes at the small-scale level, 16 communities of 40 nodes at the medium-scale level and 4 communities of 160 nodes at the large-scale level. There are two parameters; the average degree  $\bar{k}$ , which represents the density of the network, and  $\rho$ , which quantifies the separations between the three scales. We keep  $\bar{k} = 16$ , vary the parameter  $\rho = 0.05, 0.10, \dots, 2.0$  and use the program provided by Ref. [29] to generate 10 random realizations of the networks at each value of  $\rho$ .

# 6 Common statistical measures for a network

For each network, we calculate the following 16 common measures: the density (the ratio of the existing to the possible edges), the transitivity [7] (the proportion of triangles), the diameter (the maximum eccentricity), the radius (the minimum eccentricity), the degree assortativity coefficient [21], the global efficiency [20], the number of connected parts, the average number of triangles that include a node as a vertex, the average local efficiency [20], the average edge betweenness centrality [5], the average node betweenness centrality [10], the average node closeness centrality [10], the average eccentricity, the average shortest paths, and the average degree centrality [10]. We normalize the measures in the range of  $[0, 1]$  using the min-max normalization (i.e.  $f = (f - f_{\min}) / (f_{\max} - f_{\min})$ , where  $f_{\min}, f_{\max}$  are the minimum and the maximum values of a measure in the data).

# 7 Graph kernel methods

We describe the graph kernel methods used in the main text. These graph kernels are based on random walks (KStepRW, GeometricRW, ExponentialRW) [14, 11], paths (ShortestPath [2]), limited-sized subgraphs (Graphlet [4]) and subtree patterns (Weisfeiler–Lehman [25]). The implementations of these graph kernels can be found in Ref. [27].

## 7.1 KStepRW kernel

To measure the similarity between two graphs, the random walk graph kernel computes the number of equal-length walks in two graphs. Given two unlabeled graphs  $\mathcal{G}$  and  $\mathcal{G}'$  with their vertex and edge sets as  $(\mathcal{V}, \mathcal{E})$  and  $(\mathcal{V}', \mathcal{E}')$ , respectively, the direct product graph  $\mathcal{G}_\times = (\mathcal{V}_\times, \mathcal{E}_\times)$  of  $\mathcal{G}$  and  $\mathcal{G}'$  is a graph with the node set  $\mathcal{V}_\times = \{(v, v') \mid v \in \mathcal{V}, v' \in \mathcal{V}'\}$  and the edge set  $\mathcal{E}_\times = \{((v_a, v'_a), (v_b, v'_b)) \mid (v_a, v_b) \in \mathcal{E}, (v'_a, v'_b) \in \mathcal{E}'\}$ . The KStepRW kernel is the  $k$ -step random walk kernel  $\mathcal{K}_\times^k$  defined as

$$\mathcal{K}_\times^k(\mathcal{G}, \mathcal{G}') = \sum_{i,j=1}^{|\mathcal{V}_\times|} \sum_{m=0}^k [\lambda_m \mathbf{W}_\times^m]_{ij}, \quad (\text{S28})$$

where  $\mathbf{W}_\times$  is a weight matrix of  $\mathcal{G}_\times$  and  $\lambda_0, \dots, \lambda_k$  is a sequence of positive, real-valued weights. In our experiments, we set  $k = 2$  and  $\lambda_0 = \lambda_1 = \lambda_2 = 1.0$ .

## 7.2 GeometricRW kernel

GeometricRW kernel is a specific case of the  $k$ -step random walk kernel, when  $k$  goes to infinity and the weights are the geometric series, i.e.  $\lambda_m = \lambda^m$  ( $\lambda = 0.05$  in our experiments). The GeometricRW kernel is defined as

$$\mathcal{K}_{\text{GR}}(\mathcal{G}, \mathcal{G}') = \sum_{i,j=1}^{|\mathcal{V}_\times|} \sum_{m=0}^{\infty} [\lambda^m \mathbf{W}_\times^m]_{ij} = \sum_{i,j=1}^{|\mathcal{V}_\times|} [(\mathbf{I} - \lambda \mathbf{W}_\times)^{-1}]_{ij}, \quad (\text{S29})$$

where  $\mathbf{I}$  is an identity matrix of size  $|\mathcal{V}_\times| \times |\mathcal{V}_\times|$ .

## 7.3 ExponentialRW kernel

ExponentialRW kernel is a specific case of the  $k$ -step random walk kernel, when  $k$  goes to infinity and the weights are the exponential series, i.e.  $\lambda_m = \frac{\beta^m}{m!}$  ( $\beta = 0.1$  in our experiments). The ExponentialRW kernel is defined as

$$\mathcal{K}_{\text{ER}}(\mathcal{G}, \mathcal{G}') = \sum_{i,j=1}^{|\mathcal{V}_\times|} \sum_{m=0}^{\infty} \left[ \frac{(\beta \mathbf{W}_\times)^m}{m!} \right]_{ij} = \sum_{i,j=1}^{|\mathcal{V}_\times|} [e^{\beta \mathbf{W}_\times}]_{ij}. \quad (\text{S30})$$

## 7.4 ShortestPath kernel

ShortestPath kernel compares all pairs of the shortest path lengths from  $\mathcal{G}$  and  $\mathcal{G}'$  defined as

$$\mathcal{K}_{\text{SP}}(\mathcal{G}, \mathcal{G}') = \sum_{v_i, v_j \in \mathcal{G}} \sum_{v'_k, v'_l \in \mathcal{G}'} \delta(d(v_i, v_j), d(v'_k, v'_l)), \quad (\text{S31})$$

where  $d(v_i, v_j)$  and  $d(v'_k, v'_l)$  are the lengths of the shortest path between nodes  $v_i$  and  $v_j$  in  $\mathcal{G}$ , and the shortest path between nodes  $v'_k$  and  $v'_l$  in  $\mathcal{G}'$ , respectively. Here, the  $\delta$ -function is defined as  $\delta(x, y) = 1$  if  $x = y$ , and 0 if  $x \neq y$ .

## 7.5 Graphlet kernel

A size- $k$  graphlet is an induced and non-isomorphic sub-graph of size  $k$ . Let  $\mathcal{S}_k = \{G_1, \dots, G_{N_k}\}$  be a set of size- $k$  graphlets, where  $N_k$  denotes the number of unique graphlets of size  $k$ . For an unlabeled graph  $\mathcal{G}$ , we define a vector  $\mathbf{f}_\mathcal{G}$  of length  $N_k$  such that the  $i^{\text{th}}$  component of  $\mathbf{f}_\mathcal{G}$  denotes the frequency of graphlet  $G_i$  appearing as a subgraph of  $\mathcal{G}$ . Given two unlabeled graphs  $\mathcal{G}$  and  $\mathcal{G}'$ , the graphlet kernel is defined as

$$\mathcal{K}_{\text{GK}}(\mathcal{G}, \mathcal{G}') = \langle \mathbf{f}_\mathcal{G}, \mathbf{f}_{\mathcal{G}'} \rangle, \quad (\text{S32})$$

where  $\langle \cdot, \cdot \rangle$  represents the Euclidean dot product. In our experiments, we set  $k = 4$  for MUTAG, BZR, DHFR and FRANKENSTEIN datasets and  $k = 3$  for the other datasets.

## 7.6 Weisfeiler–Lehman kernel

Weisfeiler–Lehman kernel decomposes a graph into its subtree patterns and compares these patterns in two graphs. For an unlabeled graph  $\mathcal{G}$ , all vertexes  $v$  of  $\mathcal{G}$  are initialized with label  $\phi(v) = 0$ . We iterate over each vertex  $v$  and its neighbour to create a multiset label as  $\phi^{(i)}(v)$  such that  $\phi^{(1)}(v) = \phi(v)$ , and  $\phi^{(i)}$  with  $i > 1$  is defined as  $\phi^{(i)}(v) = (\phi^{(i-1)}(v), \mathbf{Q}_v^{(i-1)})$ , where  $\mathbf{Q}_v^{(i-1)}$  is the sorted labels of  $v$ 's neighbours. To measure the similarity between graphs, we count the co-occurrences of the labels in both graphs for  $h$  iterations with the kernel defined as

$$\mathcal{K}_{\text{WL}}(\mathcal{G}, \mathcal{G}') = \langle \mathbf{1}_\mathcal{G}, \mathbf{1}_{\mathcal{G}'} \rangle. \quad (\text{S33})$$

Here,  $\mathbf{1}_\mathcal{G}$  is the vector concatenation of  $h$  vertex label histograms  $\mathbf{1}_\mathcal{G}^{(1)}, \dots, \mathbf{1}_\mathcal{G}^{(h)}$  in  $h$  iterations. We set  $h = 5$  in our experiments.

TABLE S1. Summary statistics of the real-world network data.

Dataset	Number of networks	Number of classes	Number of networks in each class	Average number of nodes	Average number of edges
MUTAG	188	2	(63,125)	17.93	19.79
BZR	405	2	(319, 86)	35.75	38.36
COX2	467	2	(365, 102)	41.22	43.45
DHFR	756	2	(295, 461)	42.43	44.54
FRANKENSTEIN	4337	2	(2401, 1936)	16.90	17.88
PROTEINS	1113	2	(663, 450)	39.06	72.82
NCI1	4110	2	(2053, 2057)	29.87	32.30
NCI109	4127	2	(2048, 2079)	29.68	32.13
IMDB-BINARY	1000	2	(500, 500)	19.77	96.53
IMDB-MULTI	1500	3	(500, 500, 500)	13.00	65.94

## 8 Real-world network data

For the classification task, we test on ten real-world network datasets of bioinformatics and social networks [16]. Table S1 shows the aggregate statistics for these datasets.

The first dataset is MUTAG [8]; it consists of 188 networks of chemical compounds divided into two classes according to their mutagenic effect on a bacterium, i.e. mutagenic aromatic and heteroaromatic nitro compounds.

BZR, COX2, DHFR [28] datasets consist of 405 ligands for the benzodiazepine receptor (BZR), 467 cyclooxygenase-2 inhibitors (COX2) and 756 inhibitors of the dihydrofolate reductase (DHFR) come with 3D coordinates. In each of these datasets, the chemical compounds are divided into active and inactive compounds that we need to classify.

FRANKENSTEIN [23] is a modified version of BURSI [15] dataset made of 4337 molecules with 2401 mutagens and 1936 nonmutagens to classify. Each molecule is represented as a small network whose vertices are labelled by the chemical atom symbol and edges by the bond type.

PROTEINS [3] is a dataset of 1113 proteins represented as networks, where the nodes are secondary structure elements and the edges represent the neighbourhood within the 3-D structure or along the amino acid chain. We classify the proteins into enzymes and non-enzymes.

NCI1 and NCI109 [30] are datasets of chemical compounds with 4110 and 4127 compounds, respectively. We classify the compounds with the ability to suppress or inhibit the growth of a panel of human tumour cell lines.

IMDB-BINARY [32] is a dataset of 1000 movie collaboration ego-networks for each actor (actress) in Action and Romance genres from IMDB.com. For each network, two nodes representing actors or actresses are connected if they appear in the same movie. The task is to identify whether a given ego-network of an actor (actress) belongs to the Action or Comedy genre.

IMDB-MULTI [32] is the multi-class version of IMDB-BINARY and contains 1500 ego-networks belonging to Comedy, Romance and Sci-Fi genres.

## 9 Phase transition for Girvan-Newman networks and Lancichinetti-Fortunato-Radicchi networks

In Girvan-Newman (GN) and Lancichinetti-Fortunato-Radicchi (LFR) models, there are variations in the topological scales of the network as  $r$  ( $= p_{out}/p_{in}$ ) and  $\mu$  vary from 0 (four separate groups) to 1 (a purely random graph). We detect the transition point for the series of networks obtained when increasing  $r$  as  $r_1 = 0.01, r_2 = 0.02, \dots, r_{100} = 1.0$  (GN model) and  $\mu$  as  $\mu_1 = 0.01, \mu_2 = 0.02, \dots, \mu_{100} = 1.0$  (LFR model). For each network, we compute the three-dimensional persistence diagrams for one-dimensional holes with timescale values  $\tau_1 = 1, \dots, \tau_{100} = 100$ . We use the kernel Fisher discriminant ratio to detect the transition point for the series of the three-dimensional persistence diagrams of these networks. We obtain the phase transition at  $r = 0.12$  (Fig. S2) and  $\mu = 0.26$  (Fig. S3). These values correspond to the boundaries between the identifiable phases, where parameters can be identified from the kernel space, and the non-identifiable phases (Fig. 2(a)(b)).

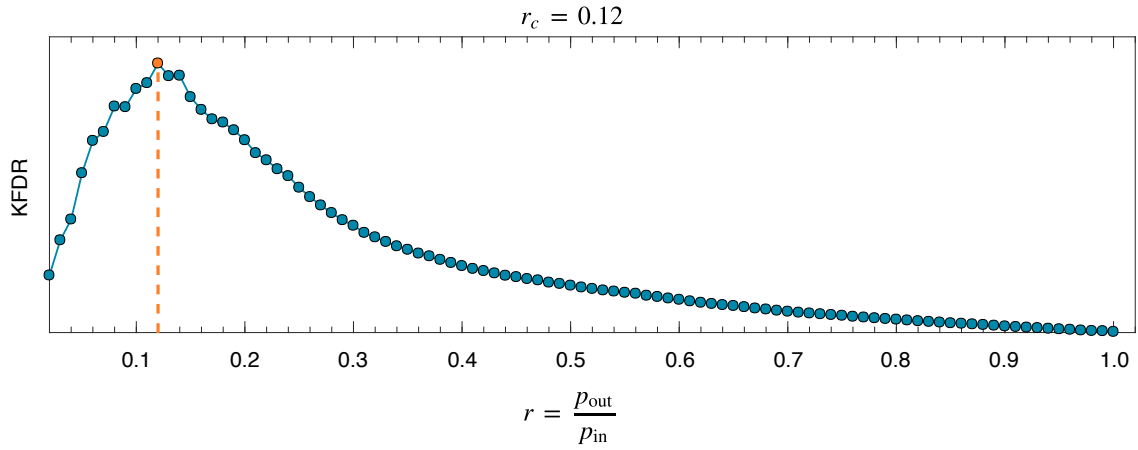


FIG. S2. **Kernel Fisher discriminant ratio (KFDR) estimated for the series of Girvan–Newman networks.** We detect the transition point in the series of 100 persistence diagrams for one-dimensional holes obtained when increasing  $r = p_{\text{out}}/p_{\text{in}}$  as  $r_1 = 0.01, r_2 = 0.02, \dots, r_{100} = 1.0$ . The maximum value of KFDR is marked with the orange point. The transition point  $r_c = 0.12$  is the value of  $r$  that achieves the maximum KFDR.

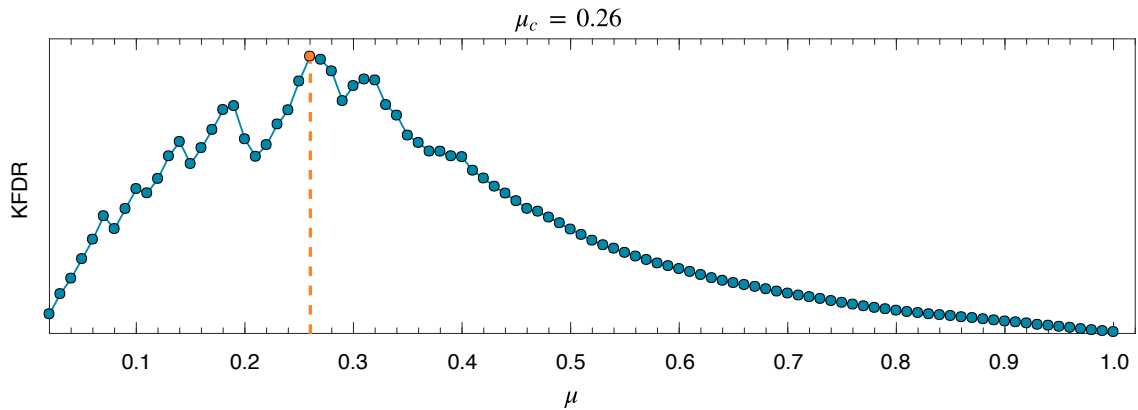


FIG. S3. **Kernel Fisher discriminant ratio (KFDR) estimated for the series of Lancichinetti–Fortunato–Radicchi networks.** We detect the transition point in the series of 100 persistence diagrams for one-dimensional holes obtained when increasing  $\mu$  as  $\mu_1 = 0.01, \mu_2 = 0.02, \dots, \mu_{100} = 1.0$ . The maximum value of KFDR is marked with the orange point. The transition point  $\mu_c = 0.26$  is the value of  $\mu$  that achieves the maximum KFDR.

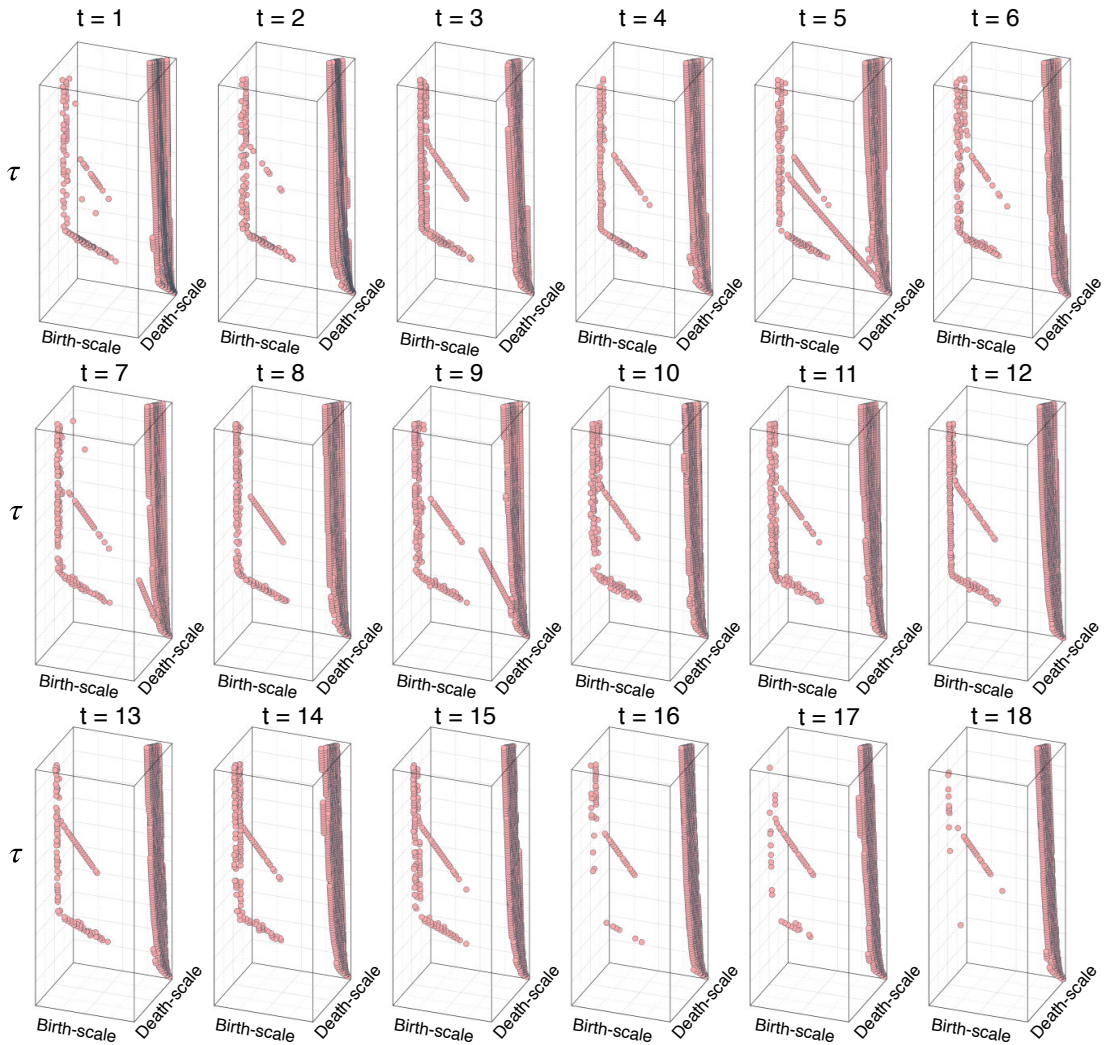


FIG. S4. Three-dimensional persistence diagrams of one-dimensional holes for the *Drosophila Melanogaster* gene regulatory networks spanning from  $t = 1$  to  $t = 18$ . For each network at each time point, we compute three-dimensional persistence diagrams with timescale values  $\tau_1 = 1, \tau_2 = 2, \dots, \tau_{100} = 100$ . The birth-scale and the death-scale axes of the diagrams are represented at the logarithmic scale.

## 10 Three-dimensional persistence diagrams for *Drosophila Melanogaster* gene regulatory networks

We use a genome-wide microarray profiling that revealed the expression patterns of 4028 genes simultaneously measured during the development of *Drosophila Melanogaster* [1]. Based on Ref. [33], 66 time points are chosen from the full developmental cycle, i.e. the embryonic stage (time points 1–30), the larval stage (time points 31–40), the pupal stage (time points 41–58) and the adulthood stage (time points 59–66). Along with Ref. [26], the time-evolving gene regulatory networks are constructed for 588 genes, which are known to be related to the developmental process based on their gene ontologies. For each gene regulatory network, we compute the three-dimensional persistence diagrams for one-dimensional holes with timescale values  $\tau_1 = 1, \dots, \tau_{100} = 100$ . Figures S4–S7 depict the three-dimensional persistence diagrams of *Drosophila Melanogaster* gene regulatory networks at full time points ranging from  $t = 1$  to  $t = 66$ .

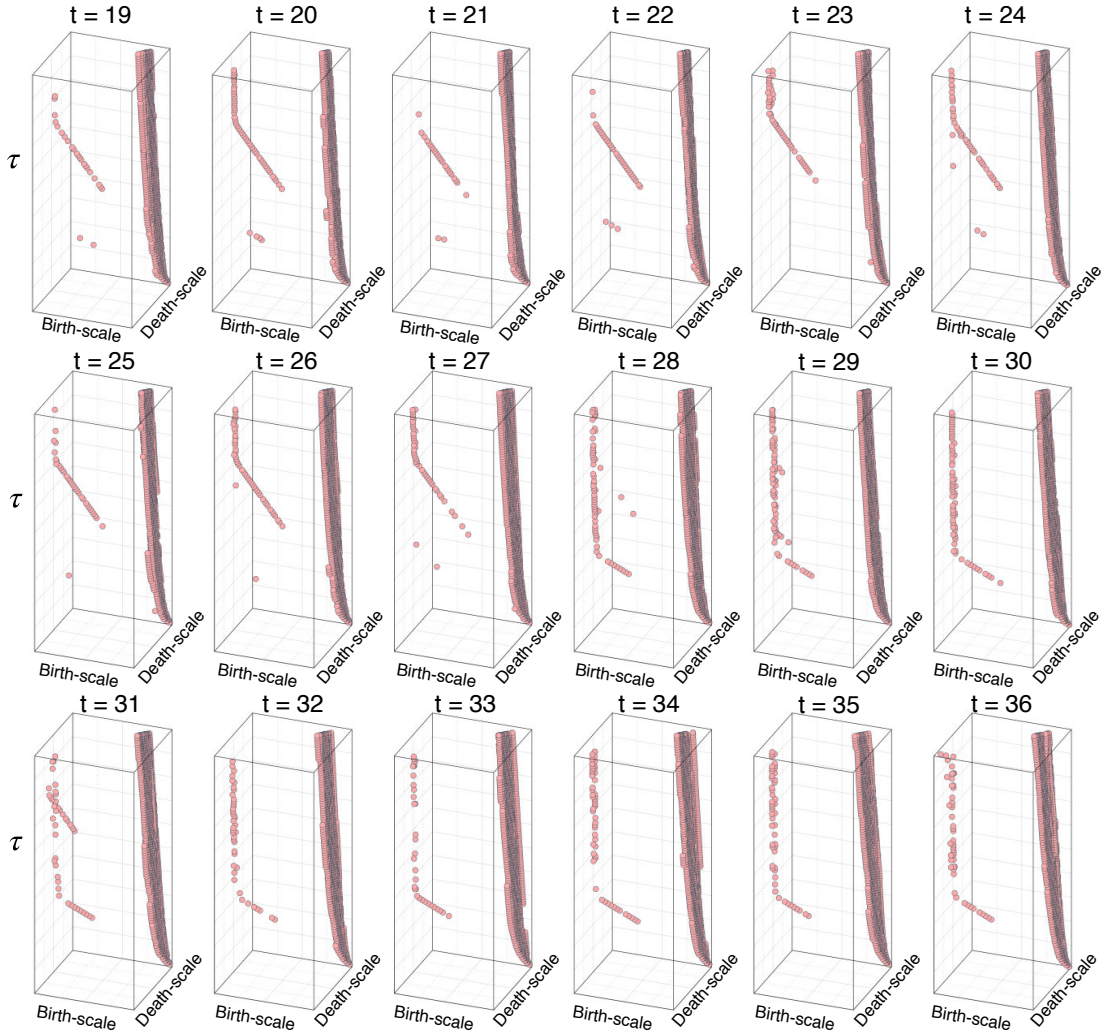


FIG. S5. Three-dimensional persistence diagrams of one-dimensional holes for the *Drosophila Melanogaster* gene regulatory networks spanning from  $t = 19$  to  $t = 36$ . For each network at each time point, we compute three-dimensional persistence diagrams with timescale values  $\tau_1 = 1, \tau_2 = 2, \dots, \tau_{100} = 100$ . The birth-scale and the death-scale axes of the diagrams are represented at the logarithmic scale.

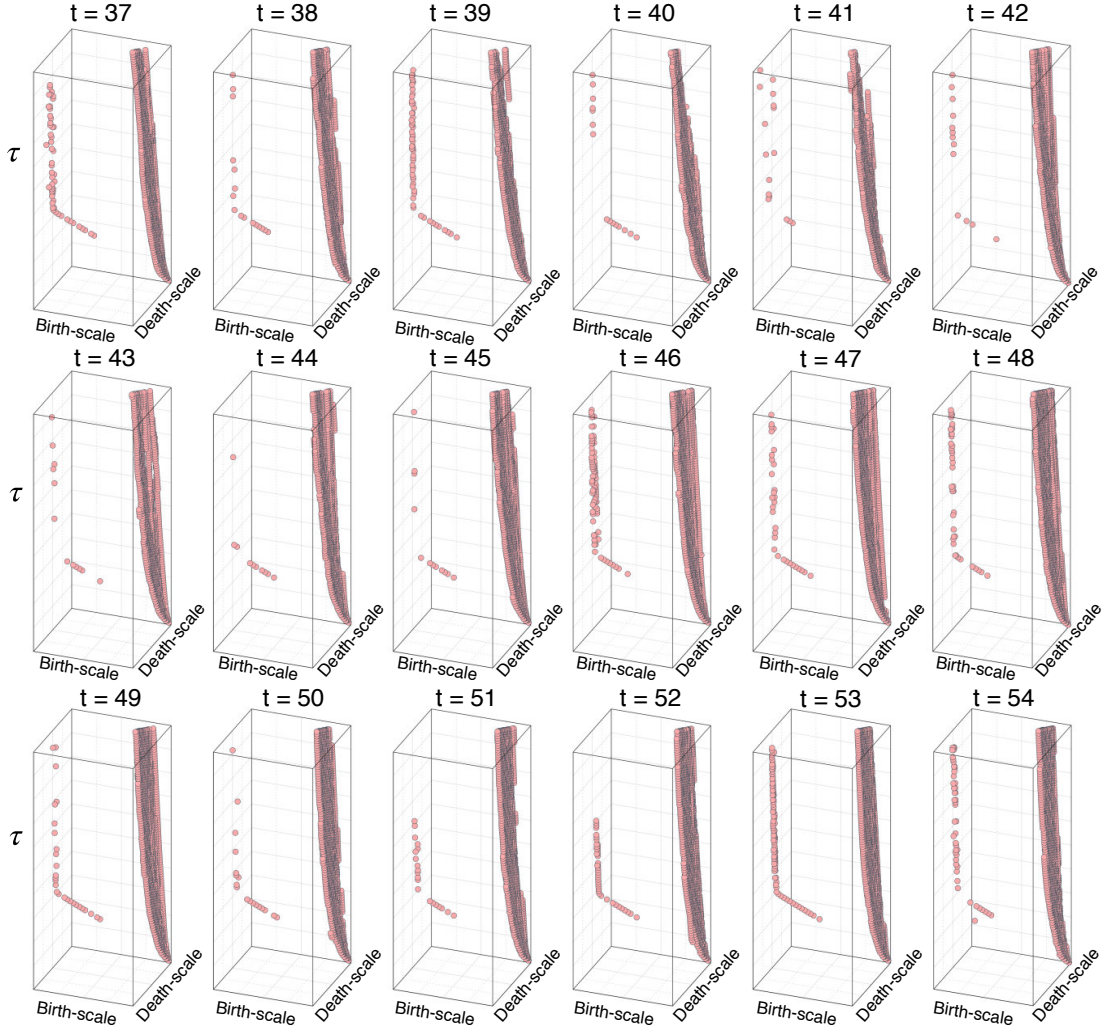


FIG. S6. **Three-dimensional persistence diagrams of one-dimensional holes for the *Drosophila Melanogaster* gene regulatory networks spanning from  $t = 37$  to  $t = 54$ .** For each network at each time point, we compute three-dimensional persistence diagrams with timescale values  $\tau_1 = 1, \tau_2 = 2, \dots, \tau_{100} = 100$ . The birth-scale and the death-scale axes of the diagrams are represented at the logarithmic scale.

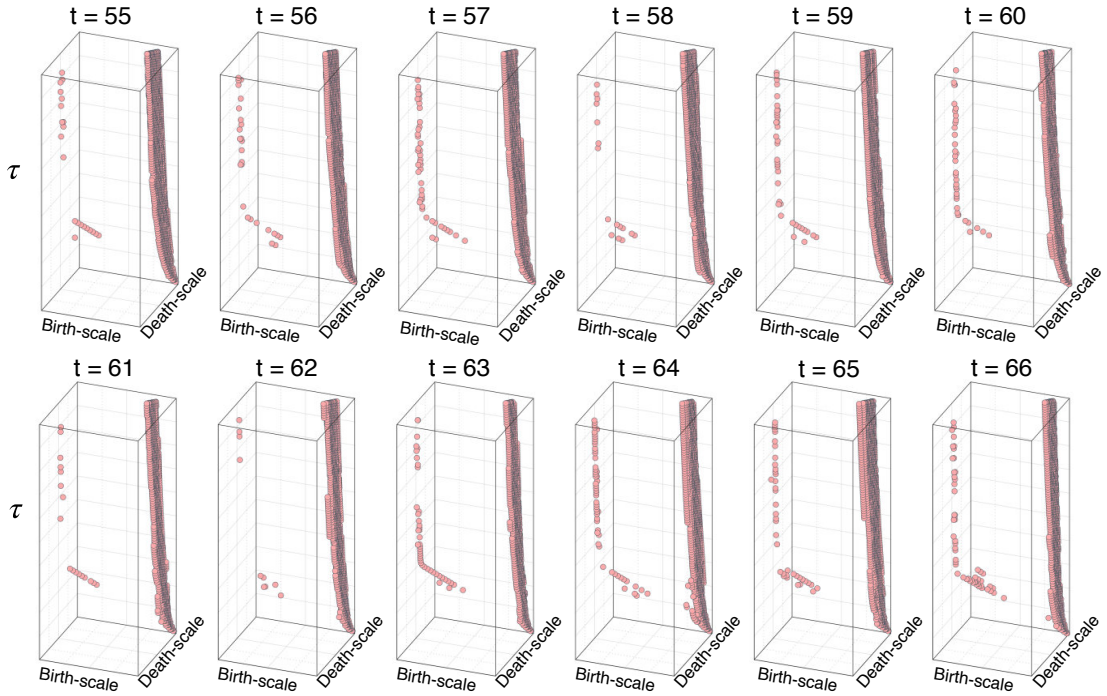


FIG. S7. Three-dimensional persistence diagrams of one-dimensional holes for the *Drosophila Melanogaster* gene regulatory networks spanning from  $t = 55$  to  $t = 66$ . For each network at each time point, we compute three-dimensional persistence diagrams with timescale values  $\tau_1 = 1, \tau_2 = 2, \dots, \tau_{100} = 100$ . The birth-scale and the death-scale axes of the diagrams are represented at the logarithmic scale.

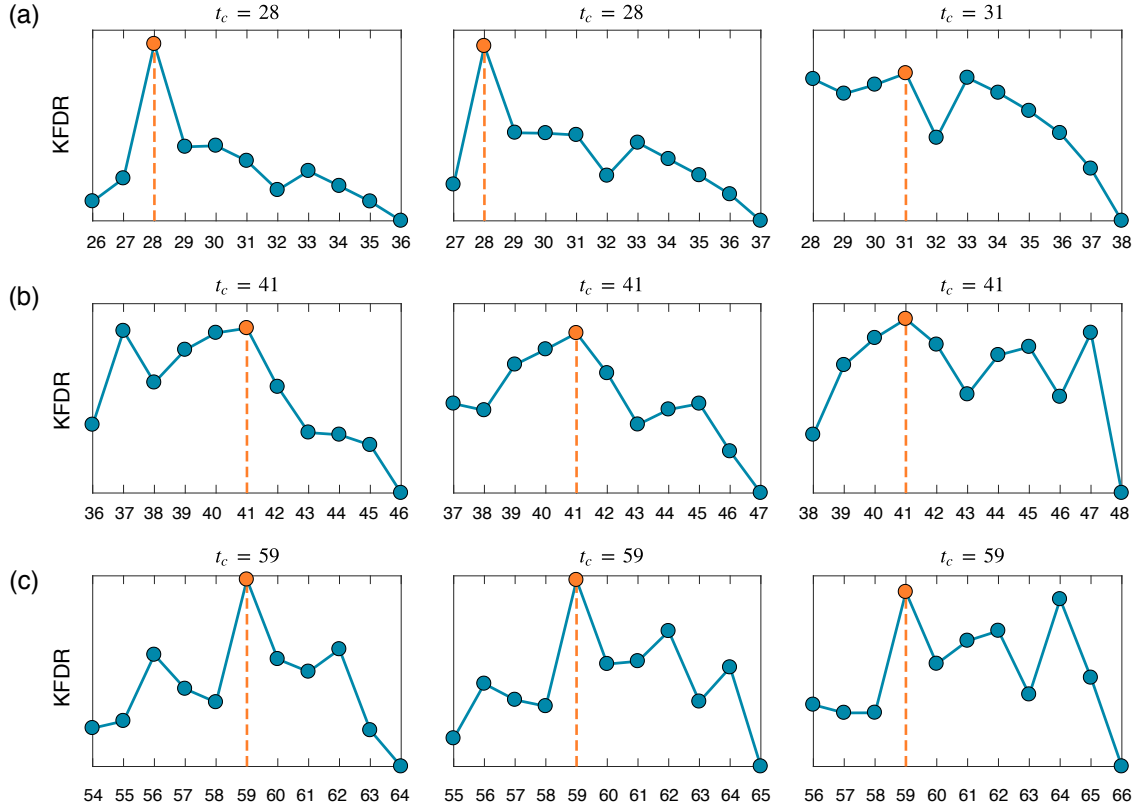


FIG. S8. **Kernel Fisher discriminant ratio (KFDR) calculated from the three-dimensional persistence diagrams of one-dimensional holes for the time-evolving *Drosophila Melanogaster* gene regulatory networks.** We detect the transition time points in the sliding windows of networks at consecutive time points spanning between two different developmental stages. In each window, the transition time point  $t_c$  is the time index of the maximum KFDR value marked with the orange point. **(a)** The windows from the embryonic stage to the larval stage with time points  $26 \rightarrow 36$  ( $t_c = 28$ ),  $27 \rightarrow 37$  ( $t_c = 28$ ) and  $28 \rightarrow 38$  ( $t_c = 31$ ). **(b)** The windows from the larval stage to the pupal stage with time points  $36 \rightarrow 46$  ( $t_c = 41$ ),  $37 \rightarrow 47$  ( $t_c = 41$ ) and  $38 \rightarrow 48$  ( $t_c = 41$ ). **(c)** The windows from the pupal stage to the adulthood stage with time points  $54 \rightarrow 64$  ( $t_c = 59$ ),  $55 \rightarrow 65$  ( $t_c = 59$ ) and  $56 \rightarrow 66$  ( $t_c = 59$ ).

## 11 Transition points in the developmental stages of *Drosophila Melanogaster* gene regulatory networks

We consider sliding windows of networks spanning between two different developmental stages. In each window, we compute the kernel Fisher discriminant ratio [13] for each time point from the three-dimensional persistence diagrams of networks in the window. The time point of the maximum ratio in each window is identified as the transition time point  $t_c$ . In our experiment, each sliding window has 11 networks. From the embryonic stage to the larval stage, we consider the windows with networks at time points  $26 \rightarrow 36$ ,  $27 \rightarrow 37$  and  $28 \rightarrow 38$ . From the larval stage to the pupal stage, we consider the windows with networks at time points  $36 \rightarrow 46$ ,  $37 \rightarrow 47$  and  $38 \rightarrow 48$ . From the pupal stage to the adulthood stage, we consider the windows with networks at time points  $54 \rightarrow 64$ ,  $55 \rightarrow 65$  and  $56 \rightarrow 66$ . From the embryonic stage to the larval stage (Fig. S8(a)), we obtain the transition time points as  $t_c = 28$  and  $t_c = 31$ , which are relatively close to the experimentally known transition time point  $t = 31$  from the profiling. From the larval stage to the pupal stage (Fig. S8(b)) and from the pupal stage to the adulthood stage (Fig. S8(c)), we obtain the transition time points as  $t_c = 41$  and  $t_c = 59$ , respectively. These points agree with the experimentally known transition time points. Our results suggest that our framework can detect transition points in dynamic time-evolving networks using the network structures alone.

## References

- [1] M. N. Arbeitman, E. E. Furlong, F. Imam, E. Johnson, B. H. Null, B. S. Baker, M. A. Krasnow, M. P. Scott, R. W. Davis, and K. P. White. Gene expression during the life cycle of drosophila melanogaster. *Science*, 297(5590):2270–2275, 2002.
- [2] K. M. Borgwardt and H.-P. Kriegel. Shortest-path kernels on graphs. In *Proc. 5th IEEE Int. Conf. Data Mining (ICDM)*, pages 74–81, 2005.
- [3] K. M. Borgwardt, C. S. Ong, S. Schönauer, S. Vishwanathan, A. J. Smola, and H.-P. Kriegel. Protein function prediction via graph kernels. *Bioinformatics*, 21(1):i47–i56, 2005.
- [4] K. M. Borgwardt, T. Petri, S. Vishwanathan, and H.-P. Kriegel. An efficient sampling scheme for comparison of large graphs. In *Proc. Mining and Learning with Graphs (MLG)*, 2007.
- [5] U. Brandes. On variants of shortest-path betweenness centrality and their generic computation. *Soc. Networks*, 30(2):136–145, 2008.
- [6] F. Chazal, V. de Silva, and S. Oudot. Persistence stability for geometric complexes. *Geometriae Dedicata*, 173(1):193–214, Dec 2014.
- [7] L. d. F. Costa, F. A. Rodrigues, G. Travieso, and P. R. Villas Boas. Characterization of complex networks: A survey of measurements. *Adv. Phys.*, 56(1):167–242, 2007.
- [8] A. K. Debnath, R. L. Lopez de Compadre, G. Debnath, A. J. Shusterman, and C. Hansch. Structure-activity relationship of mutagenic aromatic and heteroaromatic nitro compounds. Correlation with molecular orbital energies and hydrophobicity. *J. Med. Chem.*, 34(2):786–797, 1991.
- [9] P. Erdős and A. Rényi. On random graphs I. *Publ. Math.*, 6:290–297, 1959.
- [10] L. C. Freeman. Centrality in social networks conceptual clarification. *Soc. Networks*, 1(3):215–239, 1978.
- [11] T. Gärtner, P. Flach, and S. Wrobel. On graph kernels: Hardness results and efficient alternatives. In *Proc. 16th Annual Conf. Computational Learning Theory*, pages 129–143, 2003.
- [12] G. H. Golub and C. F. Van Loan. *Matrix computations*, volume 3. JHU Press, 2012.
- [13] Z. Harchaoui, E. Moulines, and F. R. Bach. Kernel change-point analysis. In *Adv. Neural Inf. Process. Syst. 21 (NIPS)*, pages 609–616, 2009.
- [14] H. Kashima, K. Tsuda, and A. Inokuchi. Marginalized kernels between labeled graphs. In *Proc. 20th Int. Conf. Machine Learning (ICML)*, pages 321–328, 2003.
- [15] J. Kazius, R. McGuire, and R. Bursi. Derivation and validation of toxicophores for mutagenicity prediction. *J. Med. Chem.*, 48(1):312–320, 2005.
- [16] K. Kersting, N. M. Kriege, C. Morris, P. Mutzel, and M. Neumann. Benchmark data sets for graph kernels, 2016. <http://graphkernels.cs.tu-dortmund.de>.
- [17] A. Lancichinetti and S. Fortunato. Benchmarks for testing community detection algorithms on directed and weighted graphs with overlapping communities. *Phys. Rev. E*, 80:016118, Jul 2009.
- [18] A. Lancichinetti, S. Fortunato, and J. Kertész. Detecting the overlapping and hierarchical community structure in complex networks. *New J. Phys.*, 11(3):033015, 2009.
- [19] A. Lancichinetti, S. Fortunato, and F. Radicchi. Benchmark graphs for testing community detection algorithms. *Phys. Rev. E*, 78:046110, Oct 2008.
- [20] V. Latora and M. Marchiori. Efficient behavior of small-world networks. *Phys. Rev. Lett.*, 87(19):198701, 2001.
- [21] M. E. J. Newman. Assortative mixing in networks. *Phys. Rev. Lett.*, 89(20):208701, 2002.
- [22] M. E. J. Newman and M. Girvan. Finding and evaluating community structure in networks. *Phys. Rev. E*, 69:026113, Feb 2004.
- [23] F. Orsini, P. Frasconi, and L. De Raedt. Graph invariant kernels. In *Proc. 24th Int. Joint Conf. Artificial Intelligence (IJCAI)*, pages 3756–3762, 2015.

- [24] M. Sales-Pardo, R. Guimera, A. A. Moreira, and L. A. N. Amaral. Extracting the hierarchical organization of complex systems. *Proc. Natl Acad. Sci. USA*, 104(39):15224–15229, 2007.
- [25] N. Shervashidze, P. Schweitzer, E. J. v. Leeuwen, K. Mehlhorn, and K. M. Borgwardt. Weisfeiler–Lehman graph kernels. *JMLR*, 12(Sep):2539–2561, 2011.
- [26] L. Song, M. Kolar, and E. P. Xing. Keller: estimating time-varying interactions between genes. *Bioinformatics*, 25(12):i128–i136, 2009.
- [27] M. Sugiyama, M. E. Ghisu, F. Llinares-López, and K. Borgwardt. graphkernels: R and python packages for graph comparison. *Bioinformatics*, 34(3):530–532, 2017.
- [28] J. J. Sutherland, L. A. O’Brien, and D. F. Weaver. Spline-fitting with a genetic algorithm: A method for developing classification structure-activity relationships. *J. Chem. Inf. Comput. Sci.*, 43(6):1906–1915, 2003.
- [29] N. Tremblay and P. Borgnat. Graph wavelets for multiscale community mining. *IEEE Trans. Signal Process.*, 62(20):5227–5239, 2014.
- [30] N. Wale, I. A. Watson, and G. Karypis. Comparison of descriptor spaces for chemical compound retrieval and classification. *Knowledge and Information Systems*, 14(3):347–375, 2008.
- [31] D. J. Watts and S. H. Strogatz. Collective dynamics of ‘small-world’ networks. *Nature*, 393(6684):440–442, 1998.
- [32] P. Yanardag and S. Vishwanathan. Deep graph kernels. In *Proc. 21th ACM SIGKDD Int. Conf. Knowledge Discovery and Data Mining (KDD)*, pages 1365–1374, 2015.
- [33] J. Zhang and J. Cao. Finding common modules in a time-varying network with application to the drosophila melanogaster gene regulation network. *J. Am. Stat. Assoc.*, 112(519):994–1008, 2017.